28. Visualizing Electronic Quantum Matter

Kazuhiro Fujita, Mohammad H. Hamidian (iD), Peter O. Sprau (iD), Stephen D. Edkins (iD), J.C. Séamus Davis (iD)

Modern quantum materials support a wide variety of exotic and unanticipated states of quantum matter and differ radically in phenomenology from conventional systems such as metals, semiconductors, band insulators, and ferromagnets. For example, quantum materials exhibit states such as electron liquid crystals, fluids of fractionalized quantum particles, quantum–entangled spin liquids, and topologically protected composite quantum particles. However, predictive theory is not fully developed for these forms of electronic quantum matter (EQM) and exploratory empirical research is required to discover and understand their properties. One of the most powerful and productive new techniques to achieve this is direct visualization of EQM at the atomic scale. For EQM, as with many highly complex systems in nature, seeing is believing and understanding. Here we describe the experimental, theoretical and analysis techniques of atomic–resolution spectroscopic imaging scanning tunneling microscopy (SI–STM) that allow such complex and enigmatic electronic/magnetic states to be directly visualized, identified, and understood.

Part D | 28

Elementary quantum particles that are massive, stable, and interacting exist in only two types: quarks and electrons. The quarks are hidden inside the nuclei of atoms meaning that, when we detect matter with our senses (excepting its inertia), we perceive only the electrons. Under most circumstances, each electron is bound within a quantum energy level of an atom or molecule and cooperative interactions with other electrons do not dominate. However, fluids formed from large numbers of unbound mutually interacting electrons do exist. The most familiar is the metallic phase of electrical conductors but there are many others. In such electronic fluids, the electrons behave individually and collectively in a fully quantum mechanical fashion. It is the amazing properties of such *electronic quantum matter* that are the focus of modern visualization studies using the technique of spectroscopic imaging scanning tunneling microscopy (SI-STM) that is introduced here.

28.1 Electrons in Crystals

Schrödinger's quantum mechanical description of a particle with mass m (e. g., an electron) is that it can exist in many wave-like states $\psi_n(x)$ each of different energy E_n. In the following introduction of general concepts, we restrict ourselves to one dimension to simplify this discussion. These states are solutions to the Schrödinger Equation

$$\left[\frac{-\hbar^2}{2m}\frac{\partial^2}{\partial x^2} + V(x)\right]\psi_n(x) = E_n\psi_n(x) , \qquad (28.1)$$

where $V(x)$ represents the potential energy of interaction of the electrons with their environment. If $V(x) = 0$, the simplest solution for a free electron is

$$\psi_{k_n}(x) = Ae^{ik_nx} \equiv A[\cos(k_nx) + i\sin(k_nx)] ;$$

$$E_n = \frac{\hbar^2k_n^2}{2m} . \qquad (28.2)$$

Thus, the quantum mechanical properties of each electron are represented by a complex-valued *wavefunction* $\psi_n(x)$, with wavelength $\lambda_n = 2\pi/k_n$ which diminishes as $1/\sqrt{E_n}$. The obvious conundrum of what such a complex field represents in a world described only by real numbers (ours), was solved by Born when he proposed that the probability to observe an electron at a given location is

$$P_n(x) = \psi_n(x)\psi_n^*(x) = |\psi_n(x)|^2 . \qquad (28.3)$$

The basic challenge of visualizing electronic quantum matter is then how to image $P(x, y, E)$ versus location $\mathbf{r} = (x, y)$ and energy E, with spatial resolution significantly better than $\lambda(E)$.

EQM visualization by SI-STM occurs directly in real space ($\mathbf{r}$-space) at the atomic scale. However, physicists also use the concept of momentum space ($\mathbf{k}$-space). This is an abstract space spanned by all possible electron wavevectors $\mathbf{k}(E) = 2\pi/\lambda(E)$ which are directly related to the electron momenta $\mathbf{p}(E) = \hbar\mathbf{k}(E)$. When EQM exists within a crystal of periodicity a, then $V(\mathbf{x})$ exhibits that same periodicity but its amplitude can range from near zero to extremely high values. Figure 28.1 shows some elementary resulting phenomena. Because of Fourier decomposition of $V(\mathbf{x})$, the basic parabolic relationship for free-electron electrons $E(\mathbf{k}) = \hbar^2\mathbf{k}^2/(2m)$ is interrupted with periodicity $j\pi/a$, where j is an integer. Here, regions of small $|\mathbf{k}| \ll \pi/a$ represent wavelengths in $\mathbf{r}$-space that are far longer than the size of each crystal unit cell, while larger $|\mathbf{k}| > \pi/a$ represent $\mathbf{r}$-space wavefunctions within the unit cell.

In $\mathbf{k}$-space, the interactions between the electrons and the crystal are thus concentrated near the reciprocal-lattice wavevectors $G_j = j\pi/a$ and, in these regions, the solution to (28.1) becomes quite different. The primary effect is the disappearance of solutions $\psi_n(\mathbf{x})$ to (28.1) within a range of energies that is roughly comparable to the amplitude of $V(\mathbf{x})$ and occurs at the wavevectors $G_j = j\pi/a$. This is referred to as the opening of *band gaps* in the $E(\mathbf{k}) = \hbar^2\mathbf{k}^2/(2m)$
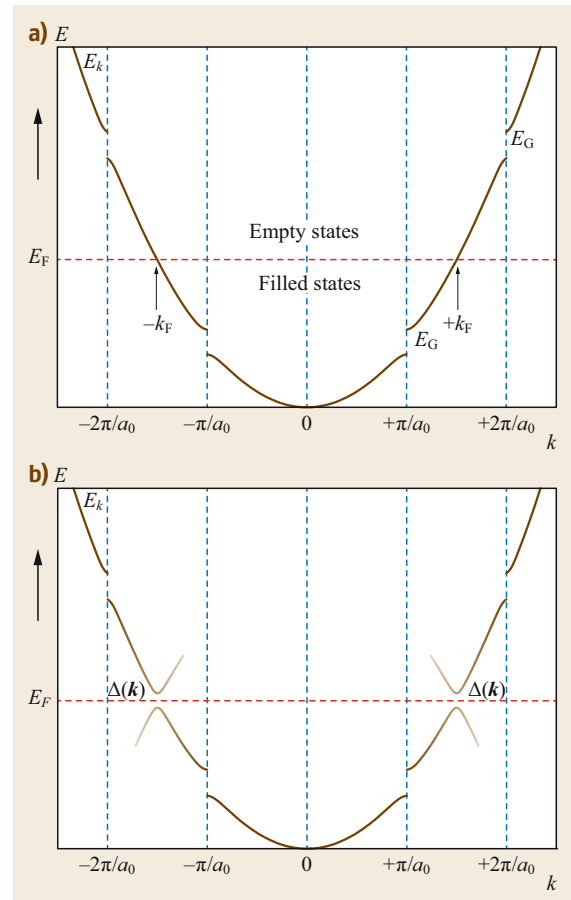

Fig. 28.1 (a) Schematic representation of the electronic band structure $k(E)$ for weakly interacting electrons in a 1-D crystalline solid. *Horizontal dashed* line is the Fermi energy E_F which separates the degenerate filled quasiparticle states $\psi_k(r, E)$ from the empty states. The band energy gaps E_G occur at the reciprocal lattice locations $G_j = \frac{j\pi}{a}$ where j is an integer and a is the crystal unit-cell dimension. **(b)** Electron–electron interactions can open an additional energy gap $\Delta(\mathbf{k})$ in the spectrum of quasiparticle states $\psi_k(r, E)$ when a new phase such as a superconductor or density-wave is formed. This energy gap $\Delta(\mathbf{k})$ can have a complicated structure in $\mathbf{k}$-space but spans the Fermi energy E_F

spectrum of free-electronic states, within which no quantum states $\psi_n(x)$ can exist.

The final key point is that electrons belong to a type of elementary particle dubbed spin-$\frac{1}{2}$ fermions. These have two spin-states with intrinsic angular momentum $\pm\hbar/2$ and thus two orientations of magnetic moment. Moreover, theory indicates that only one fermion of each spin-state can occupy any state $\psi_n(x)$. There-fore, at zero temperature in a crystal of N unit cells with M electrons per unit cell playing a role in the electronic fluid, the $NM/2$ lowest-energy states $\psi_n(x)$ are filled with electrons, and all higher energy states are empty. The energy separating the highest-energy filled state from the lowest-energy empty state is re-ferred to as the Fermi energy E_F (*dashed red line* Fig. 28.1a).

28.2 Electrons in Crystals: Disorder and Symmetry Breaking

Real crystals, even the most exquisitely prepared, do not approach the level of perfection implied by the simple solutions of (28.1). They always include several impor-tant sources of atomic-scale imperfection, all of which have the power to strongly perturb the phase of EQM in a material. Visualization of these effects plays an im-portant role in EQM studies.

First, random impurity atoms, either at crystal lat-tice sites (substitutional) or in between them (intersti-tial), exist in every real material known. The elemental identity and density of such impurity atoms is often known from the synthesis process, from analysis, or because they are substituted deliberately for research purposes.

Second, many of the most important quantum mate-rials are created by *doping* a parent compound with high proportions of atoms of another element. This usually means substituting or intercalating atoms of elements foreign to the basic crystal structure, at random lo-cations. These dopant atoms add/remove electrons to create or alter the EQM and their elemental identity is usually known. Often, the density of dopant atoms is so high that the EQM can be strongly impacted merely by their spatial arrangements.

A third source of perturbation to an EQM phase is atomic-scale disorder in the structure of the crystal lat-tice itself. This can occur in many ways, for example as vacancies at crystal lattice sites, as edge disloca-tions when parallel lines of atoms abruptly converge to a point, or as twin boundaries between orthogonal do-mains in orthorhombic crystals.

Finally, a distinct but no less consequential source of disorder can occur due to spontaneous breaking of the crystal symmetry by the EQM itself. The crystal-lographic point group is a set of symmetry operations (e. g., translations, rotations, reflections) that leave the crystal unit cell unchanged. The simplest EQM within a given crystal should satisfy the same symmetry oper-ations. Importantly, however, inter-electron interactions can generate new EQM phases that have a lower sym-metry due to spontaneous symmetry breaking, for ex-ample by breaking translational symmetry in a spatially modulating phase, or by breaking rotational symmetry and/or inversion symmetry inside each crystal unit cell.

28.3 Electrons in Crystals: Weakly to Strongly Interacting Phases

Trivial electronic fluids, such as simple metals, consist of virtually independent single-electron states $\psi_{k_n}(x)$. For such systems, Landau–Fermi liquid (LFL) theory explains how the spin, charge, and momentum ex-pected of hypothetical free-electron states are preserved even in the presence of inter-electron Coulomb inter-actions, while the dynamical properties such as the mass, magnetic moment etc. are renormalized to new values. Thus, there is a one-to-one correspondence be-tween the free-electron states of a Fermi gas (28.2) and those of the LFL system in which the renormalized states $\psi_{k_n}(x)$ are referred to as electron *quasiparti-cles*. A quantum fluid of these quasiparticles is then susceptible to several types of phase transition trig-gered by the very weak residual interactions between them. Most important and familiar among these trans-formations are to ferromagnetism [28.1], superconduc-tivity [28.2], and spin/charge density waves [28.3]. Typ-ically, in the case of superconductivity and spin/charge density waves, these residual electron–electron inter-actions open an additional energy gap $\Delta(k)$ in the spectrum of quasiparticle excitation. At its most el-ementary, the energy gap is the energy per electron required to break apart the bound electron–electron pair (Cooper pair) formed in the ground state of super-conductors, and the bound electron–hole pair (exciton) formed in the ground state of charge density waves. In fact, $\Delta(k)$ may be highly complex in k-space but always

spans the Fermi energy E_F as shown schematically in Fig. 28.1b.

Phases of EQM with weakly interacting electrons such as simple metals, dilute semiconductors, ferromagnets, conventional superconductors, and charge density waves have been well understood for many decades [28.4], and do not form the focus of the modern SI-STM research techniques that we describe in this chapter. Of more relevance and significance today, are the exotic forms of EQM generated when the electron–electron interactions become so strong that the LFL theory of metals no longer holds. The resulting fluid of electrons is strongly interacting; the states of particles are mutually correlated, fractionalized or composite, and even quantum entangled. In principle, there can be many such phases, and here we give examples of several that are the focus of present-day EQM visualization studies.

The first example of strongly correlated EQM occurs in the heavy-fermion materials. When a localized electronic state with spin-$\frac{1}{2}$ is embedded in a metal, the Kondo effect [28.5–8] screens its magnetic moment, generating a spin-less correlated quantum-many-body state. A periodic array of such magnetic atoms in a crystal lattice that are screened by hybridization with the delocalized free-electron states $\psi_{k_n}(x)$ is often referred to as a Kondo lattice. Eventually, at lowest temperatures, this hybridization process generates the famous heavy-fermion quasiparticle states [28.9–11] whose effective mass can be up to thousands of times that of a free electron. Here, the initial light k-space band $\varepsilon(k)$ is split by the hybridization into two heavy bands

$$E^{\pm}(k)$$
$$= \frac{e^{f}(k) + \varepsilon(k) \pm \sqrt{[e^{f}(k) - \varepsilon(k)]^2 + 4\Delta_{HF}^2(k)}}{2},$$
(28.4)

where $e^{f}(k)$ is the energy of the localized magnetic states typically in a partially filled f-shell, the strength of their hybridization is represented by the hybridization gap $\Delta_{HF}(k)$, and μ is the chemical potential.

A second example is the class of strongly correlated EQM that is based on the Mott insulator phase.

$$H = -t \sum_{i,j,\sigma} \left(c_{i,\sigma}^{\dagger} c_{j,\sigma} + c_{j,\sigma}^{\dagger} c_{i,\sigma} \right) + U \sum_{i} n_{i,\uparrow} n_{i,\downarrow}.$$
(28.5)

The Hubbard Hamiltonian (28.5) describes a lattice with one active orbital per site. The first term, t, represents hopping of electrons between sites i and j while the second term, U, brings the on-site Coulomb repulsion between electrons to bear. If $U/t > 8$ then the energetic cost of doubly occupying a site becomes prohibitive. At *half-filling*, when there is one electron per site and the system should be a metal (Fig. 28.1), hopping is prevented by this no double-occupancy constraint and the system converts into a strongly correlated Mott insulator [28.12] with a Mott–Hubbard energy gap $\Delta_{MH}(k)$. In more common and realistic situations where correlations are strong but multiple orbitals are active, the orbital multiplicity may allow an orbital-selective Mott phase to appear. In this recently discovered form of EQM, interorbital magnetic (Hund's) coupling of strength J suppresses the interorbital fluctuations [28.13] within each atom, and electrons associated with some orbitals can become strongly correlated or even Mott localized while coexisting with delocalized electronic quasiparticles associated with the other orbitals [28.13–16]. Mott insulators become central to modern EQM studies when they are doped away from half-filling with additional charge carriers. Many exotic phases of EQM including spin liquids [28.17, 18], and high-temperature superconductors [28.18–20] then emerge.

A related example of strongly correlated EQM has emerged in the last decade or so for the case of carrier-doped correlated insulators. Electronic liquid crystals [28.21–26] are EQM phases that, because of strong local interactions of spin and charge in carrier-doped Mott insulators, spontaneously break the point group symmetry of the crystal. If the rotational symmetry of an EQM phase is lower than that of its crystal rotations, i.e., it occurs at wavevector $Q = 0$ or intraunit cell, the phase is now usually referred to as being an electronic nematic. If the translational symmetry of an EQM phase is below that of its crystal translation symmetry, i.e., occurring at finite wavevector $Q \neq 0$ unrelated to Bragg wavevectors, the phase is variously referred to as electronic smectic or a strong-correlation density wave. A fundamental electronic liquid crystal state that has long been anticipated in superconducting doped Mott insulators [28.5–21] is a pair density wave (PDW) phase. Here the density of electron pairs modulates at finite wavevector $Q \neq 0$. Research into all these types of electronic liquid crystals is at the forefront of EQM studies today.

28.4 Spectroscopic Imaging Scanning Tunneling Microscopy

For all the above reasons, a general capability to directly visualize EQM at atomic scale would seem to hold great potential for scientific discovery. Although scanning tunneling microscopy (STM) revolutionized imaging of surfaces and nanoscale electronic objects in the 1980s and early 1990s, comprehensive visualization of the EQM within a given bulk material was not pursued then. Subsequently, however, novel STM designs were introduced which allow visualization of the complete electronic structure of a material [28.27]

in a process now dubbed spectroscopic imaging scanning tunneling microscopy (SI-STM) [28.28]. SI-STM is a powerful general tool for solid-state physics research and has opened a completely new perspective onto the structure of many novel and exotic states of EQM.

Generically, a STM functions by using a three-axis piezoelectric positioner to place the STM tip within a vertical distance z above the sample surface, typically at a specific atom of known in-plane vector location
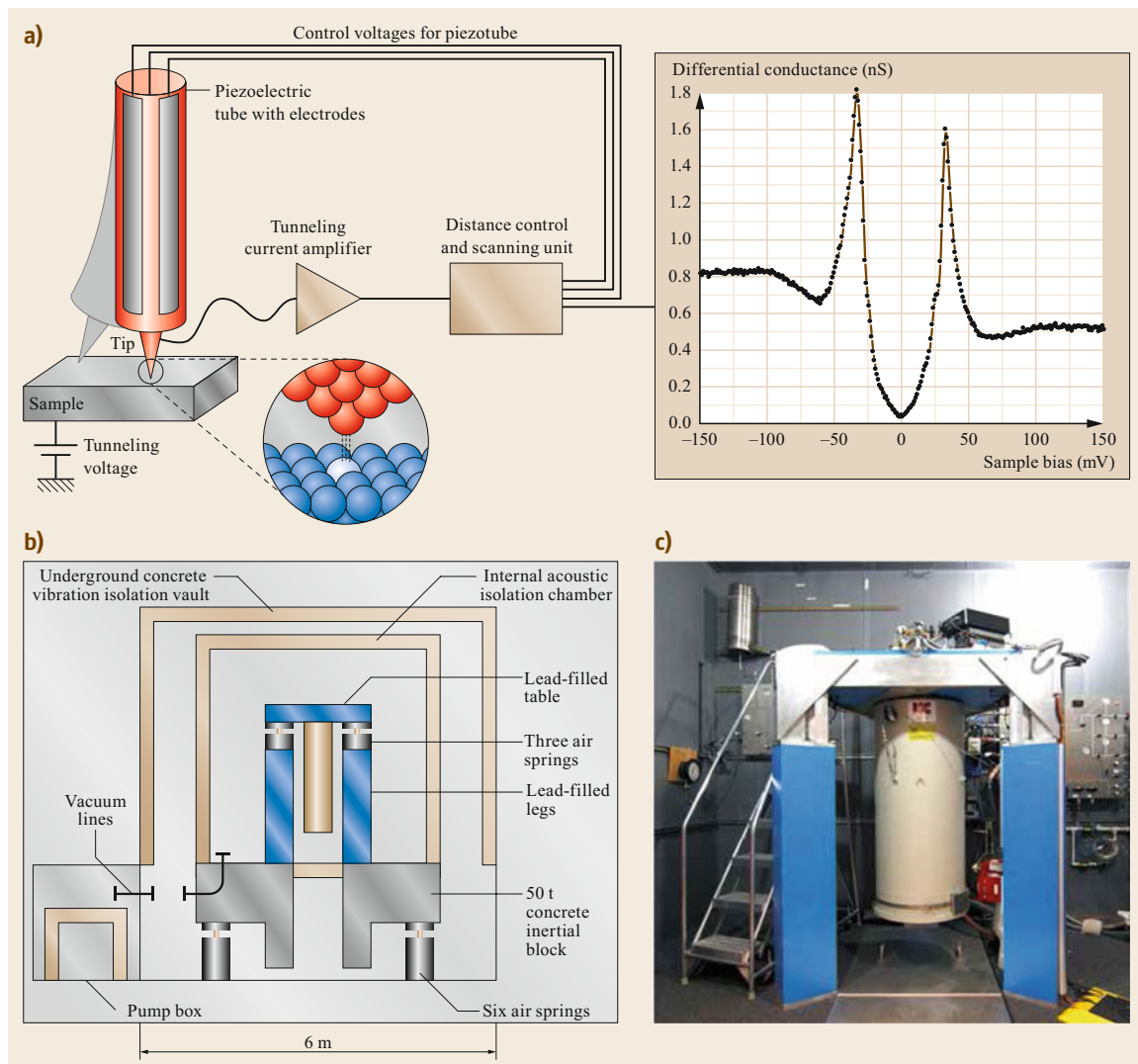

Fig. 28.2 (a) Operational schematic of SI-STM showing how the $dI/dV(\boldsymbol{r}, E)$ spectrum is measured at each atom. **(b)** Nested acoustic isolation chambers on stacked vibrational isolator stages provide the ultralow vibration environment. **(c)** Our typical ULV cryostat table supporting a custom-built ULV refrigerator to cool the SI-STM to temperatures below $T = 1$ K. Reprinted from [28.27] with the permission of AIP Publishing

r (Fig. 28.2a). Highly specialized instruments and facilities are required for SI-STM research. Most basic is the requirement for an ultralow vibration (ULV) laboratory environment so that the highest precision techniques can be deployed. Typically, in our studies we use 10^{-13} m $< z \ll 10^{-10}$ m with a requirement that random fluctuations in $\delta z \leq 10^{-14}$ m/$\sqrt{\text{Hz}}$. It is the latter that sets the ultralow vibration constraint for the laboratory, cryostat, and refrigerator. This is achieved by nesting acoustic shielding enclosures on sequential vibrational isolation platforms (Fig. 28.2b). The SI-STM instrument itself provides a final vibration isolation stage based upon its structural design and the use of a custom built subkelvin ^{3}He, or ^{3}He/^{4}He dilution, refrigerator (Fig. 28.2c).

The primary observable in all STM studies is the electron tunneling current from the STM tip to the sample. It is given by

$$I(\mathbf{r}, V) = Ce^{-\frac{T(\mathbf{r})}{T_0}} \int\limits_0^{E=eV} [f(E,T)N(\mathbf{r},E)]$$

$$\times \left[(1 - f(E,T))N_{\text{Tip}}(E) \right] \mathrm{d}E , \qquad (28.6)$$

where $T(\mathbf{r})$ is the tip–surface distance or *topograph*, V the tip–sample bias voltage, $N(\mathbf{r}, E)$ the sample's local-density-of-electronic-states, $N_{\text{Tip}}(E)$ the tip density-of-electronic-states, $Ce^{-(T(\mathbf{r}))/T_0}$ contains exponential barrier-tunneling effects of tip elevation the tip–sample work-functions and the tunneling matrix elements; $f(E,T)$ is the Fermi function. Thus, as temperature approaches zero and with $N_{\text{Tip}}(E)$ and $C(\mathbf{r})$ both equal to constants, (28.6) can be simplified as

$$I_{\text{S}} = Ce^{-\frac{T(\mathbf{r})}{T_0}} \int\limits_0^{eV_{\text{S}}} N(\mathbf{r},E)\mathrm{d}E$$

$$\Rightarrow Ce^{-\frac{T(\mathbf{r})}{T_0}} = \frac{I_{\text{S}}}{\int_0^{eV_{\text{S}}} N(\mathbf{r},E)\mathrm{d}E} , \qquad (28.7)$$

where V_{S} and I_{S} are the (constant but arbitrary) *set-up* bias voltage and current, respectively.

In practice, these two parameters fix the tip elevation $T(\mathbf{r})$ for each tip–sample junction based on the implicit solution to (28.7). Equivalently, in constant-current topographic imaging, the STM feedback system adjusts $T(\mathbf{r})$ as it scans over the sample surface to maintain a set point current, I_{S}, at a constant applied tip–sample bias V_{S}. The *topographic* image $T(\mathbf{r}, V_{\text{S}})$ can be understood by inverting (28.7) to yield

$$T(\mathbf{r}, V_{\text{S}}) = T_0 \ln \left[\int\limits_0^{E=eV_{\text{S}}} N(\mathbf{r},E)\mathrm{d}E \right] \qquad (28.8)$$

up to a constant. The essential point is that a high signal-to-noise ratio topographic image $T(\mathbf{r}, E)$ obtained by constant-current STM imaging reveals both the surface structure and a logarithmic measure of the energy-integral over $N(\mathbf{r}, E)$ for the range $0 < E < eV_{\text{s}}$.

Second, current imaging tunneling spectroscopy (CITS) [28.29, 30] is based on substitution of (28.8) into (28.6) with $f(E,T) \approx 1$ to yield

$$\frac{I(\mathbf{r}, V)}{I_{\text{s}}} = \frac{\int_0^{eV} N(\mathbf{r},E)\mathrm{d}E}{\int_0^{eV_{\text{s}}} N(\mathbf{r},E)\mathrm{d}E} . \qquad (28.9)$$

Here V is formally unrelated to V_{s} although it is typically in the range $|V| \ll |V_{\text{s}}|$. At its most useful, CITS is applied by choosing V_{S} so that $T(\mathbf{r}, V_{\text{S}})$ is virtually featureless, in which case $I(\mathbf{r}, V) \propto \int_0^{eV} N(\mathbf{r},E)\mathrm{d}E$ becomes a robust measure of the spatial structure of the density-of-electronic-states integrated over energy. However, if $T(\mathbf{r}, V_{\text{S}})$ cannot be rendered homogeneous, the ratio $I(\mathbf{r}, +V)/I(\mathbf{r}, -V)$ is often used as a valid measure of spatial symmetries of the EQM.

The central observable in modern SI-STM studies is the energy derivative of (28.7), usually referred to as the tip–sample differential conductance $\mathrm{d}I/\mathrm{d}V(\mathbf{r}, E = eV) = g(\mathbf{r}, E)$. With N_{TIP} and $C(\mathbf{r})$ both equal to constants and substituting for $Ce^{-\frac{T(\mathbf{r})}{T_0}}$ from (28.7) into the bias-voltage derivate of (28.6) one finds

$$g(\mathbf{r}, V) = \frac{eI_{\text{s}}N(\mathbf{r},E)}{\int_0^{eV_{\text{s}}} N(\mathbf{r},E)\mathrm{d}E} . \qquad (28.10)$$

Thus, the theoretically all-important $N(\mathbf{r}, E)$ of an electronic phase can, in principle, be visualized with subatomic resolution and crystal-lattice register. Again, choosing V_{S} so $T(\mathbf{r}, V_{\text{S}})$ is homogeneous renders $g(\mathbf{r}, V) = CN(\mathbf{r}, E)$ where C is a spatially invariant constant. Visualization of the spatially resolved and energy-resolved density-of-electronic-states—one of the most powerful modern tools for studies of exotic electronic matter/materials—thus becomes possible. Note that if $T(\mathbf{r}, V_{\text{S}})$ is heterogeneous, the ratio $g(\mathbf{r}, +V)/g(\mathbf{r}, -V)$ may still be used as a valid measure of spatial symmetries of the EQM.

In relating any measured $g(\mathbf{r}, V)$ at finite temperature T to the physical $N(\mathbf{r}, E)$, one must acknowledge the *thermal broadening* effect. This is an unavoidable uncertainty in the energy argument of all types of tunneling spectroscopy derived from (28.6) and is caused by the convolution of the tip and sample Fermi–Dirac distributions $f(E)(1 - f(E))$ therein. From this, the energy uncertainty of tunneling electrons is $\delta E \gtrsim 3.5 k_{\text{B}}T$ and $N(\mathbf{r}, E)$ cannot be measured with better energy resolution (e. g., $\delta E > 1.25$ meV at $T = 4.2$ K).

Beyond the r-space visualization of EQM that has become possible using SI-STM imaging of $T(r, V_S)$; $I(r, V)$; $g(r, V)$, an unexpected new research area has emerged based on Fourier analysis of these images to yield

$$T(q, V_S) = \Re\mathfrak{e}\{T(q, V_S)\} + i\Im\mathfrak{m}\{T(q, V_S)\}, \tag{28.11a}$$

$$I(q, V) = \Re\mathfrak{e}\{I(q, V)\} + i\Im\mathfrak{m}\{I(q, V)\}, \tag{28.11b}$$

$$g(q, V) = \Re\mathfrak{e}\{g(q, V)\} + i\Im\mathfrak{m}\{g(q, V)\}. \tag{28.11c}$$

All such images are complex-valued in the sense that the modulations symmetric about the origin ($\Re\mathfrak{e}$ or cosine component) are distinguishable from those that are antisymmetric ($\Im\mathfrak{m}$ or sine component). In this regard, they contain a fundamental distinction from measurements in reciprocal space by photon or neutron scattering because, to date, only real-valued intensities can be measured throughout reciprocal space in these modalities, meaning that symmetric and antisymmetric modulations cannot be discriminated. By contrast in SI-STM studies, the r-space origin can be chosen with an accuracy of ≈ 2 pm or about 0.5% of the size of a typical crystal unit cell [28.31], yielding high precision in the evaluation of complex-valued Fourier transforms [28.32–34] throughout q-space (28.11).

Again, there are technical issues that must be overcome for valid use of Fourier transforms of SI-STM data such as $T(r, V_S)$; $I(r, V)$; $g(r, V)$. For example, the k-space resolution is limited because q-space resolution during Fourier analysis to yield $T(q, V_S)$; $I(q, V)$; $g(q, V)$ is inverse to the r-space field-of-view size L in which the $T(r, V_S)$; $I(r, V)$; $g(r, V)$ were measured. Typically, to achieve a given precision in momentum $\delta k \approx \delta q/2$ requires that $g(r, V)$ be measured with $L \gtrsim \pi/\delta q$ and with energy resolution at the theoretical limit $\delta E \gtrsim 3.5 k_B T/e$. For example, to determine the wavevector k of a quasiparticle with precision $\delta k \approx 0.01\,(\pi/a)$ and energy-resolution $\delta E \approx 30\,\mu\text{eV}$ requires typically that $L \gtrsim 100\,a$ or about 40 nm square at $T \approx 0.1$ K.

A profoundly important practical issue is that picometer-scale distortions occur in the rectilinearity throughout the $g(r, V)$ data set over the continuous and extended period (up to a week or more) required for each $g(r, V)$ acquisition. To address this issue, we recently introduced/developed a postmeasurement distortion correction technique. The objective is to identify and measure a slowly varying field $u(r)$ [28.35] representing the displacement vector u of each location r in a topographic image of the crystal surface $T(r)$, from the location $r - u(r)$ where it should be if $T(r)$ were perfectly periodic. In a crystal with tetragonal symmetry, the power-spectral-density (PSD) Fourier transform of $T(r)$, $|T(q)|^2$, where $T(q, V) = \Re\mathfrak{e}\{T(q, V)\} + i\Im\mathfrak{m}\{T(q, V)\}$, then exhibits two distinct peaks representing the atomic corrugations; these are centered at the Bragg wavevectors $Q_a = (Q_{ax}, Q_{ay})$ and $Q_b = (Q_{bx}, Q_{by})$ with a and b labeling the unit-cell vectors. To proceed, $T(r)$ is multiplied by reference cosine and sine functions with periodicity set by the wavevectors Q_a and Q_b, and whose origin is chosen at a specific atomic location in $T(r)$. The resulting four images are filtered to retain q-regions within a radius $\delta q = 1/\lambda$ of the four Bragg peaks with the magnitude of λ chosen to capture only the relevant image distortions arising from piezo drift (STM tip location drift), and retain the local phase information $\theta_a(r), \theta_b(r)$ that quantifies the local displacements from perfect periodicity: $X_a(r) = A_a(r)\cos\theta_a(r)$, $Y_a(r) = A_a(r)\sin\theta_a(r)$; $X_b(r) = A_b(r)\cos\theta_b(r)$, $Y_b(r) = A_b(r)\sin\theta_b(r)$. Dividing the appropriate pairs of images yields the phase-images

$$\theta_a(r) = \tan^{-1}\frac{Y_a(r)}{X_a(r)} \quad \text{and}$$

$$\theta_b(r) = \tan^{-1}\frac{Y_b(r)}{X_b(r)}$$

(in a perfect lattice, $\theta_a(r), \theta_b(r)$ would be independent of r). Considering only the components periodic with the lattice, the measured topograph can therefore be represented by

$$\begin{aligned} T(r) \\ = T_0\left[\cos(Q_a\cdot[r+u(r)]) + \cos(Q_b\cdot[r+u(r)])\right]. \end{aligned}$$

Correcting this for the spatially dependent phases $\theta_a(r), \theta_b(r)$ generated by $u(r)$, requires an affine transformation at each (xy) that is equivalent to finding a set of local transformations which makes the $\theta_{a,b}$ take on constant values, $\overline{\theta}_a$ and $\overline{\theta}_b$ over all space. Thus, let r be a point on the unprocessed (distorted) $T(r)$, and let $\tilde{r} = r - u(r)$ be the point of equal phase on the *perfectly* lattice-periodic image which needs to be determined. This produces a set of equivalency relations

$$\begin{aligned} Q_a\cdot r + \theta_a(r) &= Q_a\cdot\tilde{r} + \overline{\theta}_a, \\ Q_b\cdot r + \theta_b(r) &= Q_b\cdot\tilde{r} + \overline{\theta}_b \end{aligned} \tag{28.12}$$

or

$$Q\begin{pmatrix}\tilde{r}_1 \\ \tilde{r}_2\end{pmatrix} = Q\begin{pmatrix}r_1 \\ r_2\end{pmatrix} - \begin{pmatrix}\overline{\theta}_a - \theta_a(r) \\ \overline{\theta}_b - \theta_b(r)\end{pmatrix},$$

$$Q = \begin{pmatrix}Q_{ax} & Q_{ay} \\ Q_{bx} & Q_{by}\end{pmatrix}. \tag{28.13}$$

Solve for the distortion-displacement field as

$$u(r) = Q^{-1} \begin{pmatrix} \overline{\theta}_a - \theta_a(r) \\ \overline{\theta}_b - \theta_b(r) \end{pmatrix} \qquad (28.14)$$

with the convention $\overline{\theta}_i = 0$ that generates a *perfect* lattice with an atomic peak at the origin. Then, by using this Lawler–Fujita technique, one can estimate $u(r)$ and thereby undo distortions to convert $T(r)$ data into a distortion-corrected topograph $T'(r)$ exhibiting the known periodicity and symmetry of the termination layer of the crystal. The key step for electronic-structure symmetry determination is then that the identical geometrical transformations to undo $u(r)$ in $T(r)$ yielding $T'(r)$, are also carried out on every $g(r, E)$ acquired simultaneously with the $T(r)$ to yield a distortion-corrected $g'(r, E)$. The $T'(r)$ and $g'(r, E)$ are then registered to each other and to the lattice with excellent periodicity. This procedure can be used quite generally with SI-STM data that exhibits appropriately high resolution in both r-space and q-space.

The full power of modern SI-STM techniques thus involves several technically complex requirements: $T(r, V_S)$; $I(r, V)$; $g(r, V)$ must be measured at sufficiently low temperatures to achieve the desired $\delta E(T)$, in large FOV sizes L sufficient to achieve the required $\delta q(L)$, and postprocesses to achieve lattice periodicity and valid phase resolution in $T(q, V_S)$; $I(q, V)$; $g(q, V)$. However, such efforts are well worthwhile because access to $T(q, V_S)$; $I(q, V)$; $g(q, V)$ data provides powerful new modalities for physics research based upon (i) quasiparticle interference imaging, (ii) spontaneous symmetry breaking in EQM, and (iii) phase-resolved energy-gap visualization of ordered states—all of which will be discussed below.

28.5 Cooper–Pair Condensate Visualization

One further novel modality in modern visualization of EQM is the use of superconducting STM tips to measure the spatial variation of Josephson tunneling, and thus to directly image the Cooper-pair condensate [28.36]. This is referred to as scanned Josephson tunneling microscopy (SJTM). As usual, there are technical challenges: consider two superconducting electrodes with superconducting energy gaps $\Delta(T)$ and phases ϕ_1 and ϕ_2, the Josephson current is given by $I(\phi) = I_J \sin(\phi)$ where $\phi = \phi_2 - \phi_1$. The Josephson critical current I_J of Cooper pairs is given by $I_J R_N = \frac{\pi \Delta(T)}{2e} \tanh\left[\Delta(T)/(2k_B T)\right]$ where R_N is the normal state junction resistance, k_B the Boltzmann constant, and $2e$ the Cooper-pair charge. For ϕ to be time independent the Josephson energy $E_J = \frac{\phi_0 I_J}{2\pi}$, where ϕ_0 is the magnetic flux quantum, must exceed the thermal fluctuation energy $k_B T$. For a nanometer-dimension Josephson junction formed between a superconducting STM tip and the surface both with $\Delta(T) \approx 1\,\mathrm{meV}$, I_J will then be in the picoamp range so that the stable phase difference regime occurs at submillikelvin temperatures that are, at present, unattainable for SI-STM.

However, imaging of phase-diffusion-dominated Josephson tunneling is possible by using a superconducting-tip STM to measure an $I(V)$ whose maximum current $I_c \propto I_J^2$ [28.36–41]. To achieve this, high Δ, low R_N, and millikelvin operating temperatures are required. Typically, a dilution refrigerator-based STM operated below $50\,\mathrm{mK}$ is used, and to achieve a high tip-energy-gap Δ_T a nanometer-sized flake of HTS is picked up on the end of a tungsten tip. This converts the measured NIS (normal metal–insulator–superconductor) tunneling spectrum to an SIS (superconductor–insulator–superconductor) spectrum exhibiting energy separation $\approx 2(\Delta_S + \Delta_T)$ between conductance peaks. Finally, the maximum observable Cooper-pair current $I_c \propto I_J^2$ is measured versus position r, with atomic resolution and register to yield $I_c(r)$ while the topographic image $T(r, V_S)$ is achieved using single-particle SIS tunneling from the same tip. Note that in SI-STM applications, an SIS junction can operate in two modes: Josephsons (two electron) or quasiparticle (single electron) tunneling. When the superconducting tip is very close to the surface a Josephson junction *JJ* forms while, when it is held at a more typical distance, a quasiparticle tunnel junction is achieved. Atomic-scale visualization of Cooper-pair condensates is then possible using $I_c(r)$ measurements with superconducting STM tips, as is determination of the q-space structure of condensates based on Fourier analysis of these images to yield

$$I_c(q, V_S) = \mathfrak{Re}\{I_c(q, V_S)\} + i\mathfrak{Im}\{I_c(q, V_S)\} \,.$$

28.6 Visualizing Effects of Individual Impurity Atoms and Dopant Atoms

Inserting a single known impurity atom at a specific crystal site and measuring the surrounding atomic-scale perturbations reveals much about the underlying electronic structure. For simple metals, this generates the classic Friedel oscillations of charge density at $q = 2k_F$, surrounding each impurity/vacancy. Pioneering studies of these Friedel oscillations and related phenomena in simple metals [28.42] and superconductors [28.43] showed beautifully how they can be visualized using SI-STM. However, for the more exotic forms of ECM at the foci of today's research, such as doped Mott insulators, spin liquids, correlated high-temperature superconductors, heavy-fermion metals, and topologically ordered phases, the equivalent phenomena are far more complex and challenging to detect and to understand.

Here, using three examples, we describe how direct visualization of the effects of individual impurity atoms in such advanced EQM phases is achieved. In general, a bound (localized) electronic *impurity state* $\psi_i(\boldsymbol{r}, E_i)$ appears surrounding each impurity/vacancy site. This new state $\psi_i(\boldsymbol{r}, E_i)$ has a specific energy E_i (or perhaps a set of quantized energies), and is neither an orbital of the impurity atom nor a native eigenstate of the electronic fluid. The value of E_i and the spatial structure of $|\psi_i(\boldsymbol{r}, E_i)|^2$ contain key information about the electronic structure and interactions of the EQM phase in which the impurity is embedded [28.44].

Cooper pairing that underpins the high-temperature superconductivity in the CuO_2 plane of cuprates can be destroyed at atomic scale by substituting a Zn impurity atom for a Cu atom. The Zn atom is spinless and strongly repulsive for electrons. In theory, this should destroy the superconductivity on the four bonds between Zn and the neighboring Cu atoms and should produce an intense impurity state whose wavefunction $\psi_{Zn}(\boldsymbol{r}, E)$ is concentrated at the four adjacent Cu sites [28.45]. For Zn-doped $Bi_2Sr_2CaCu_2O_{8+x}$, a typical $g(\boldsymbol{r}, E)$ of a 5-nm-square region (Fig. 28.3a) at $V = -1.5\,\text{mV}$ is shown in Fig. 28.3b and contains the distinct four-fold symmetric shape and orientation expected for $\psi_{Zn}(\boldsymbol{r}, E)$. Figure 28.3c shows a comparison between spectra taken at $\psi_{Zn}(\boldsymbol{r}, E)$ center and at usual superconducting regions of the sample, revealing a very strong intragap conductance peak at energy $E = -1.2\,\text{meV}$. And, at these sites, the superconducting coherence peaks are strongly diminished, indicating the suppression of superconductivity. All of these phenomena are among the theoretically predicted characteristics of strong interactions at a single impurity atom in a d-wave superconductor [28.44].

In a related example, when an individual Ni impurity atom is substituted for a Cu atom in cuprates $N(\boldsymbol{r}, E)$ should exhibit two impurity states as expected of a magnetic atom [28.46]. Studies at Ni sites (Fig. 28.3d–f) reveal two impurity states $\psi_{Ni}(\boldsymbol{r}, E)$ in $g(\boldsymbol{r}, E = eV)$ maps. One occurs at $V = \pm 9\,\text{mV}$ (Fig. 28.3f) and the other at $V = \pm 19\,\text{mV}$ and each contains particle-like and hole-like components. The inset shows the typical spectra taken at the Ni atom site in which there are two clear particle-like $g(\boldsymbol{r}, E)$ peaks. The existence of two impurity states is as expected for a magnetic impurity in a d-wave superconductor, because there are two spin configurations [28.44]. Perhaps most significant, however, is that the magnetic impurity does not appear to suppress the superconductivity (as judged by the coherence peaks) at all, as if magnetism is not destructive to the pairing interaction locally.

The third example is of correlated high-temperature superconductivity in the FeAs(Se) planes of Fe-based high-temperature superconductors. These systems should also support strong-correlation impurity states as in Fig. 28.3g–i. However, the situation is more complex because these materials are typically strongly nematic in that the electronic structure breaks 90° rotation symmetry, probably due to magnetic interactions. Thus, the crystal symmetry is already reduced to orthorhombic at high temperatures before the superconductivity appears. In this situation, a very strong impurity state $\psi_{vac}(\boldsymbol{r}, E)$ occurs at a vacancy at the Fe site in the FeAs or FeSe plane. Indeed, for virtually all families of these compounds a striking impurity state referred to as a *dimer* is reported throughout the literature typically associated with a vacancy or substitution on the Fe site. Figure 28.3g shows the location of such a vacancy as detected at the Se termination layer of FeSe. Figure 28.3h shows that the spatial structure of $\psi_{vac}(\boldsymbol{r}, E)$ does indeed consist of a sharp double-peaked structure with a vacancy at its center (Fig. 28.3i).

There is another fundamentally important population of impurity atoms in many of the most important EQM phases and advanced materials. These are the dopant atoms that are introduced during synthesis to convert the material from its parent state to whatever is the structure or phase required for study and application. Simultaneous visualization of dopant atom populations and their impact on local electronic structure are therefore of profound interest. Thus, because the visualization of these dopant populations is most relevant to the impact they have on the spatial structure of the ordered phases they create, we defer this discussion to Sect. 28.9.
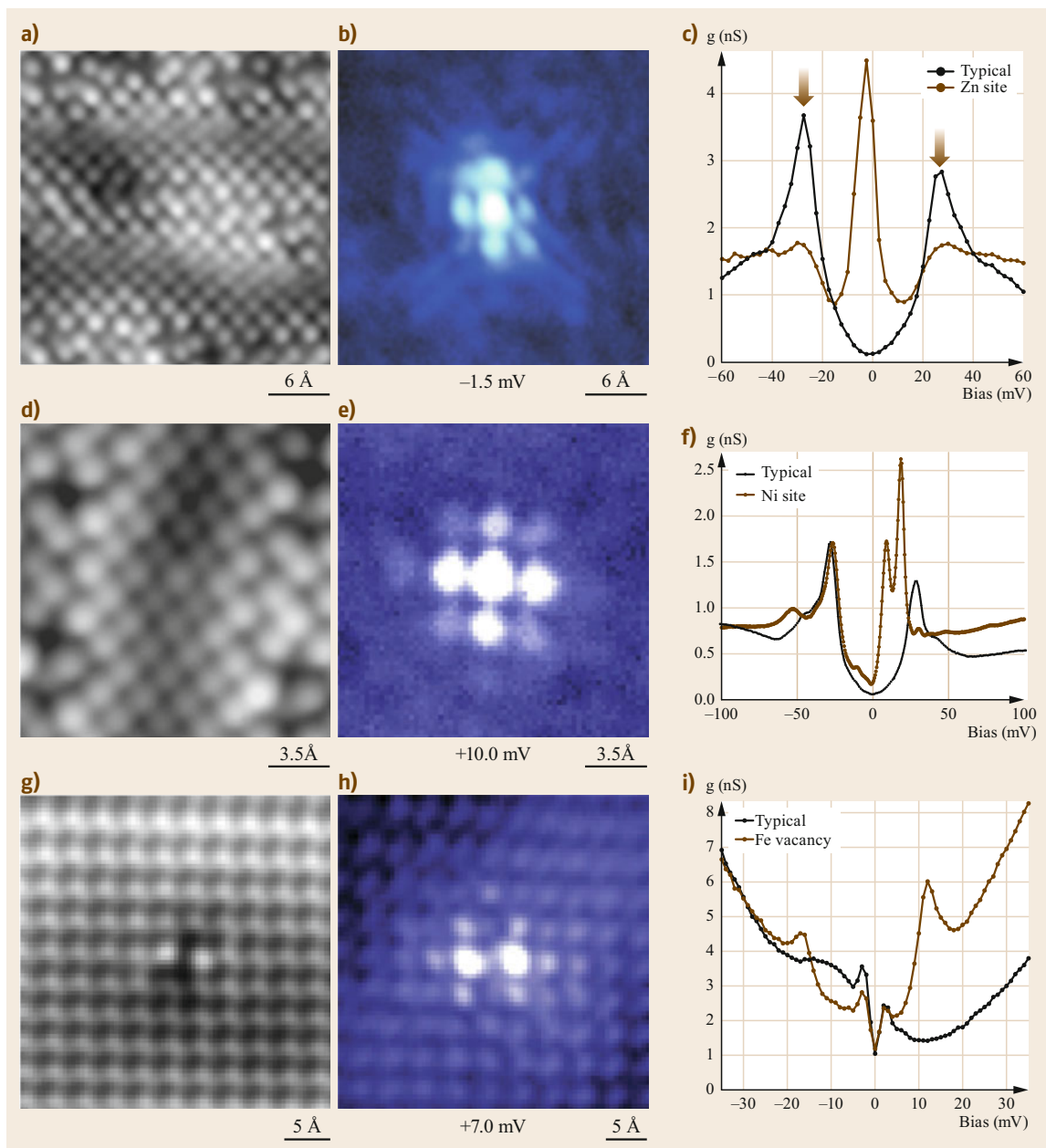
Fig. 28.3 (a) Topograph of a BiO termination layer centered on a Zn site. **(b)** Local density of states at $-1.5\,mV$ in the same FOV as **(a)**. **(c)** Impurity-state $\psi_{Zn}(r, E)$ due to the effect on superconductivity of the Zn substitution atom at a Cu site in the CuO_2 plane. From [28.45]. **(d)** Topograph of a BiO termination layer centered on an Ni site. **(e)** Local density of states at $+10\,mV$ in the same FOV as **(d)**. **(f)** Impurity-state $\psi_{Ni}(r, E)$ due to the effect on superconductivity of the Ni substitution atom at a Cu site in the CuO_2 plane. From [28.46]. **(g)** Topograph of an Se termination layer centered on a vacancy site. **(h)** Local density of states at $+7\,mV$ in the same FOV as **(g)**. **(i)** Impurity-state $\psi_{vac}(r, E)$ at a vacancy/substitution atom at an Fe site in the Fe plane of FeSe

28.7 Quasiparticle Interference Imaging

Quasiparticle scattering interference [28.47, 48] (QPI) occurs when an impurity atom/vacancy scatters quasiparticles which then interfere to produce characteristic modulations of the density-of-states $\delta N(\boldsymbol{r}, E)$ surrounding each impurity site. QPI has become widely used to determine exotic electronic structure of correlated electronic materials. Impurity scattering is usually studied by using $\delta N(\boldsymbol{q}, E)$, the square root of the power-spectral-density Fourier transform of the perturbation to the density of states by the impurity

$$\delta N(\boldsymbol{q}, \omega) = -1/\pi \operatorname{Tr} \left(\mathfrak{Im} \left\{ \sum_{\boldsymbol{k}} G(\boldsymbol{k}, \omega + \mathrm{i}\delta) S(\omega) \right. \right.$$
$$\left. \left. \times G(\boldsymbol{k} + \boldsymbol{q}, \omega + \mathrm{i}\delta) \right\} \right) .$$

$$(28.15a)$$

Here $G(\boldsymbol{k}, \mathrm{i}\omega)$ is the electron propagator $G(\boldsymbol{k}, \mathrm{i}\omega) = 1/[\mathrm{i}\omega - E_0(\boldsymbol{k}) - \Sigma(\boldsymbol{k}, \mathrm{i}\omega)]$ of a quasiparticle state $|\boldsymbol{k}\rangle$ with momentum $\hbar\boldsymbol{k}$, and $\Sigma(\boldsymbol{k}, \mathrm{i}\omega) = \mathfrak{Re}\{\Sigma(\boldsymbol{k}, \mathrm{i}\omega)\} + \mathrm{i}\mathfrak{Im}\{\Sigma(\boldsymbol{k}, \mathrm{i}\omega)\}$ is the self-energy of interacting electrons. The $S(\omega)$ is a matrix representing all the possible scattering processes between states $|\boldsymbol{k}\rangle$ and $|\boldsymbol{k} + \boldsymbol{q}\rangle$. Atomic-scale imaging of these interference patterns $\delta N(\boldsymbol{r}, E)$ is achieved using spatial mapping of $g(\boldsymbol{r}, E)$. This approach, now generally dubbed QPI, has developed into a high-precision technique for measurement of electronic band structure $E_i(\boldsymbol{k})$ of strongly correlated electron fluids [28.49–54].

Interpretation of QPI often requires modeling the expected phenomena using the full structure of (28.15). However, the predictions of the simpler Born approximation are more easily understood. Here, if the $\boldsymbol{r}$-space structure of the scattering potential is represented by its Fourier transform $V(\boldsymbol{q})$, the simplified prediction is

$$\delta N(\boldsymbol{q}, E) = \left(-\frac{V(\boldsymbol{q})}{\pi} \right) \mathfrak{Im}\{\Lambda(\boldsymbol{q}, E)\},$$
$$\Lambda(\boldsymbol{q}, E) = \int \mathrm{d}^2 r e^{-\mathrm{i}\boldsymbol{q}\cdot\boldsymbol{r}} G(\boldsymbol{r}, E) G(-\boldsymbol{r}, E) . \quad (28.15b)$$

This means that the QPI power-spectral-density $|g(\boldsymbol{q}, \mathrm{E})|^2$ can be regarded as proportional to the product of the scatterer structure factor $|V(\boldsymbol{q})|^2$ and $|\mathfrak{Im}\{\Lambda(\boldsymbol{q}, E)\}|^2$ which is a property only of the band structure $E_i(\boldsymbol{k})$. The QPI technique has proven particularly powerful because it can achieve energy resolution $\delta E < 30\,\mu\mathrm{eV}$, it is equally sensitive to empty $(E > E_\mathrm{F})$ as to filled $(E < E_\mathrm{F})$ states, and it works perfectly well in high magnetic fields.

Figure 28.4a shows a schematic image of the perturbations to the density of states $\delta N(\boldsymbol{r}, E)$ due to a random distribution of impurity atoms; surrounding each impurity is the Friedel oscillation which occurs in this simple situation at wavelength $\lambda(E) = 2\pi/(q(E)); q(E) = 2k(E)$. Figure 28.4b shows the amplitude Fourier transform of Fig. 28.4a from which $q(E)$ is measured for this E; Fig. 28.4c shows the procedure for reconstruction of $k(E)$ from measured $q(E)$. This generic procedure to extract the band structure $E(\boldsymbol{k})$ from QPI data in $g(\boldsymbol{r}, E)$ can now be carried out reliably for one- and two-
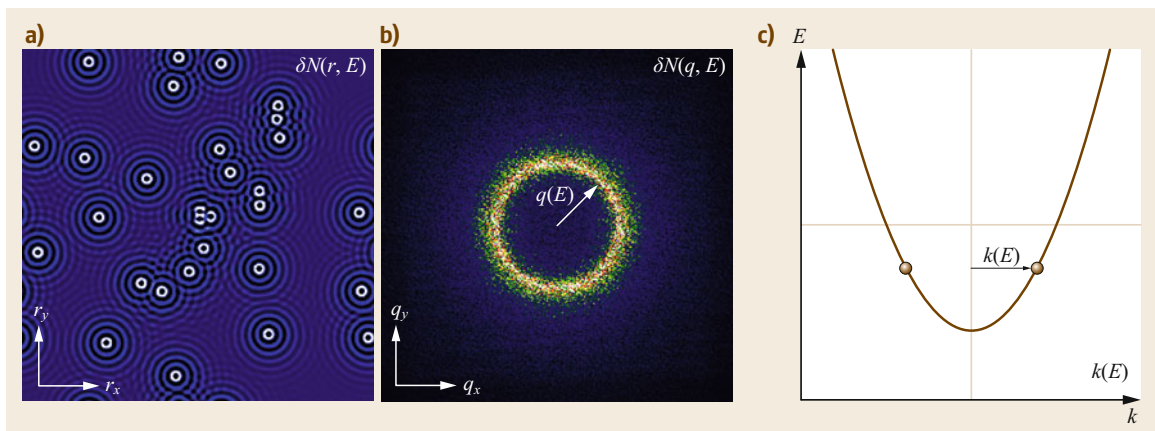
Fig. 28.4 (a) Schematic diagram of scattering interference patterns in $\delta N(\boldsymbol{r}, E)$ (Friedel oscillations) due to random distributions of impurity atoms in a simple/uncorrelated 2-D metal. **(b)** The $|\delta N(\boldsymbol{q}, E)|$ derived from A showing that the magnitude of all the QPI wavelengths |q| is the same. **(c)** From B and using a band structure model (here a 2-D parabolic band) one can recover $\boldsymbol{k}(E)$ of the momentum-space electronic eigenstates of the metal

band systems $E_i(\boldsymbol{k})$; $i = 1, 2$, and reasonably reliably for three bands.

In this chapter, we explain how to use the QPI technique to detect and to understand the $E_i(\boldsymbol{k})$ for strongly interacting/correlated forms of EQM. We use as examples three classes of materials with strong electronic correlations and/or exotic $E_i(\boldsymbol{k})$ that are at the focus of EQM research worldwide: heavy-fermion metals, metallic surface states of ordered topological insulators (TI), and orbital-selective Hund's metals.

Heavy fermions are composite fermions generated by hybridization of free electrons and localized f-

electron spins; the expected splitting of a light band into two extremely heavy bands by the interaction with localized f-electron magnetic moments is described by (28.4). Techniques to visualize heavy fermions are relatively new. Although first proposed in the 1980s this heavy band structure had never been observed directly, both because energy resolution $\delta E < 100\,\mu eV$ was required to detect the extremely slow evolution $\boldsymbol{k}(E)$ and because much of the phenomenology occurs $E > E_F$ which is inaccessible to photoemission. A dilution-refrigerator-based SI-STM system is required to achieve $\delta E < 100\,\mu eV$ and to image such

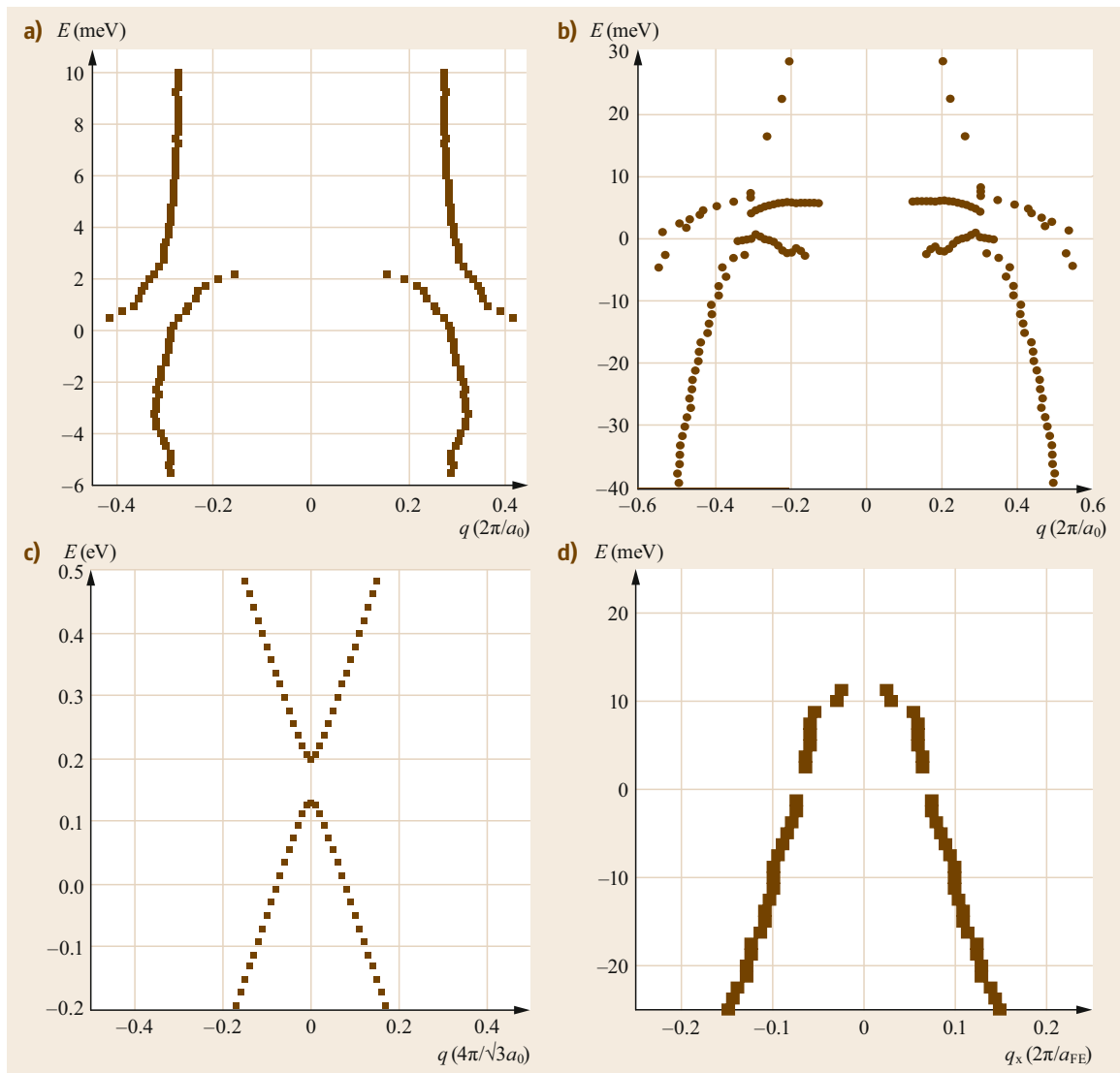**Fig. 28.5** **(a)** QPI-measured heavy-fermion band structure $E_i(\boldsymbol{k})$, $i = 1, 2$ for URu_2Si_2. **(b)** QPI-measured heavy-fermion band structure $E_i(\boldsymbol{k})$ $i = 1, 2$ for $CeCoIn_5$. **(c)** QPI-measured Dirac-mass gapped band structure $E_i(\boldsymbol{k})$ $i = 1, 2$ for $Cr(BiSb)_2Te_3$. **(d)** QPI-measured Hund's metal band structure $E_i(\boldsymbol{k})$ for FeSe

heavy-fermion QPI. Figure 28.5a shows the QPI-measured dispersion of $E_i(\boldsymbol{k})$ for both heavy bands of URu_2Si_2 [28.51], a heavy-electron material where $m^* = 27m_e$, by using this technique. Just as anticipated by (28.4), the QPI maxima evolve towards smaller $\boldsymbol{q}$-radius but then abruptly jump to a larger $\boldsymbol{q}$-radius from whence they diminish back towards smaller radii and eventually merge with the light band structure.

A second example of the same approach is the canonical heavy-fermion superconductor $CeCoIn_5$. Its heavy QPI was studied similarly by using a ^{3}He-refrigerator-based SI-STM at 250 mK and, within the energy-range $-4\,\text{meV} < E < +12\,\text{meV}$, the onset of hybridization can be detected as a rapid evolution of the maximum QPI intensity features towards smaller $\boldsymbol{q}$-radius, followed by an abrupt jump to a larger $\boldsymbol{q}$-radius, followed by a second rapid diminution of QPI $\boldsymbol{q}$-radii. The $E_i(\boldsymbol{k})$ for both heavy bands derived from these data are shown in Fig. 28.5b, and are all as expected for the heavy-fermion bands within the hybridization-gap $-4\,\text{meV} < \Delta_{HF} < +12\,\text{meV}$.

EQM with distinct topological characteristics are now of wide interest. In topological insulators (TI), spin-orbit interactions generate a spectrum of linearly dispersing weakly interacting surface states that are spin-momentum locked and, by now, extremely well understood [28.55]. However, for topological surface/edge states in the presence of an ordered phase such as ferromagnetism or superconductivity, theory predicts extraordinary new types of electronic phenomena. An excellent example of how to determine the surface states of an ordered topological material is in the QPI studies of surface states of the ferromagnetic topological insulator (FMTI) $Cr_x(Bi_{0.1}Sb_{0.9})_{2-x}Te_3$ [28.56]. In this canonical FMTI material, by imaging the surface-state $g(\boldsymbol{r}, E)$ from above E_F to well below, the QPI data reveal the appearance of the Dirac-mass gap starting at $E \approx +130\,\text{meV}$ as shown in Fig. 28.5c. With increasing E, the surface-state QPI signature evolves smoothly and with diminishing $|\boldsymbol{q}|$ until $\boldsymbol{q} = 0$ is reached just above $E \approx 130\,\text{meV}$. At this point, the surface-state QPI disappear near $\boldsymbol{q} = 0$. Just below $E \approx 200\,\text{meV}$, the surface-state QPI signatures reappear once again, emerging from $\boldsymbol{q} = 0$. These data represent two surface-state bands

$$E_\pm(\boldsymbol{k}) = E_D \pm \sqrt{(\hbar v)^2 k^2 + \Delta_{FM}^2}\,,$$

meaning that the energy range devoid of QPI between the two band edges is twice the Dirac-mass gap.

A unique new metallic state, the strongly correlated Hund's metal [28.57, 58], has recently been predicted using multiorbital strong-correlation Hubbard models. These consider the intraorbital Hubbard energy U, the interorbital Coulomb interaction energy U', and the interorbital Hund's interaction energy J aligning spins. For a range of strong J, dynamical mean-field theory [28.20] predicts that interorbital charge fluctuations are greatly suppressed leading to an orbital decoupling of the strong correlations. This means that in the same metal the quasiparticles associated with some atomic orbitals may be weakly correlated (noninteracting), while those associated with other orbitals on the same atom may be very strongly correlated (to the point of extinction). Because Fe-based superconducting materials are excellent candidates to exhibit Hund's metal [28.59] effects, FeSe serves as a good example of orbital-selective quasiparticle scattering interference imaging. Figure 28.5d shows the measured dispersion of QPI intensity maxima for this material.

28.8 Momentum–Space Imaging of Energy Gaps of Ordered Phases: Superconductivity

If, for a given electron–electron interaction potential $V_{SC}(\boldsymbol{k})$ and a given band structure $E_{\boldsymbol{k}}$, a solution exists for the Bardeen–Cooper–Schrieffer (BCS) equation

$$\Delta_{\boldsymbol{k}} = -\sum_{\boldsymbol{p}} V_{SC}(\boldsymbol{p} - \boldsymbol{k}) \left[\frac{\Delta_{\boldsymbol{p}}}{2\Omega_{\boldsymbol{p}}} \tanh\left(\frac{\Omega_{\boldsymbol{p}}}{2k_B T} \right) \right],$$
$$\Omega_{\boldsymbol{k}} = \sqrt{(E_{\boldsymbol{k}})^2 + (\Delta_{\boldsymbol{k}})^2}$$

(28.16)

then a superconducting state forms. The energy gap $\Delta(\boldsymbol{k})$ opens symmetrically across the Fermi energy but can be highly anisotropic in $\boldsymbol{k}$-space so that quasiparticles $\psi_{\boldsymbol{k}}(E)$ are detectable in the energy-range $\Delta(\boldsymbol{k})^{min} < E < \Delta(\boldsymbol{k})^{max}$. Within this range, impurity scattering of superconducting (Bogoliubov) quasiparticles produces characteristic modulations of $N(\boldsymbol{r}, E)$. The quasiparticle-dispersion $E_i(\boldsymbol{k})$ exhibits closed constant energy contours (CEC) that are roughly *banana-shaped* and surround Fermi surface $\boldsymbol{k}$-points where $\Delta(\boldsymbol{k})^{min}$ occurs. Then, at a given energy $\Delta(\boldsymbol{k})^{min} < E < \Delta(\boldsymbol{k})^{max}$, the locus of the *banana tips* can be determined because the maximum intensity of scattering-induced $\delta N(\boldsymbol{r}, E)$ modulations occurs at wavevectors $\boldsymbol{q}_j(E)$ connecting them. The superconductor's Cooper-pairing en-

ergy gap $\Delta(\mathbf{k})$ is then determined directly by geometrically inverting [28.60, 61] the measured set $\mathbf{q}_j(E)$ in the energy-range $\Delta(\mathbf{k})^{\min} < E < \Delta(\mathbf{k})^{\max}$. Below we give examples of how this technique is used to determine the $\mathbf{k}$-space structure of superconducting energy-gaps $\Delta(\mathbf{k})$ using examples of different materials.

Determination of $\Delta(\mathbf{k})$ in cuprates e.g., $Bi_2Sr_2CaCu_2O_8$ is based on the dispersive $\delta N(\mathbf{q}, E) \propto$ $\delta g(\mathbf{q}, E)$ modulations at wavevectors $\mathbf{q}_j(E)$ as shown in Fig. 28.6a (*left*). Given the predominantly tetragonal nature of the crystal and single-band structure, four zeros in the $\Delta(\mathbf{k})$ along the $(\pm 1, \pm 1)$ directions are consistent with the observed *octet* of $\mathbf{q}_j(E)$ maxima. Inverting set $\mathbf{q}_j(E)$ in the energy-range $0 < E < \Delta(\mathbf{k})^{\max}$ gives the gap structure shown in Fig. 28.6a (*right*) [28.62–64].
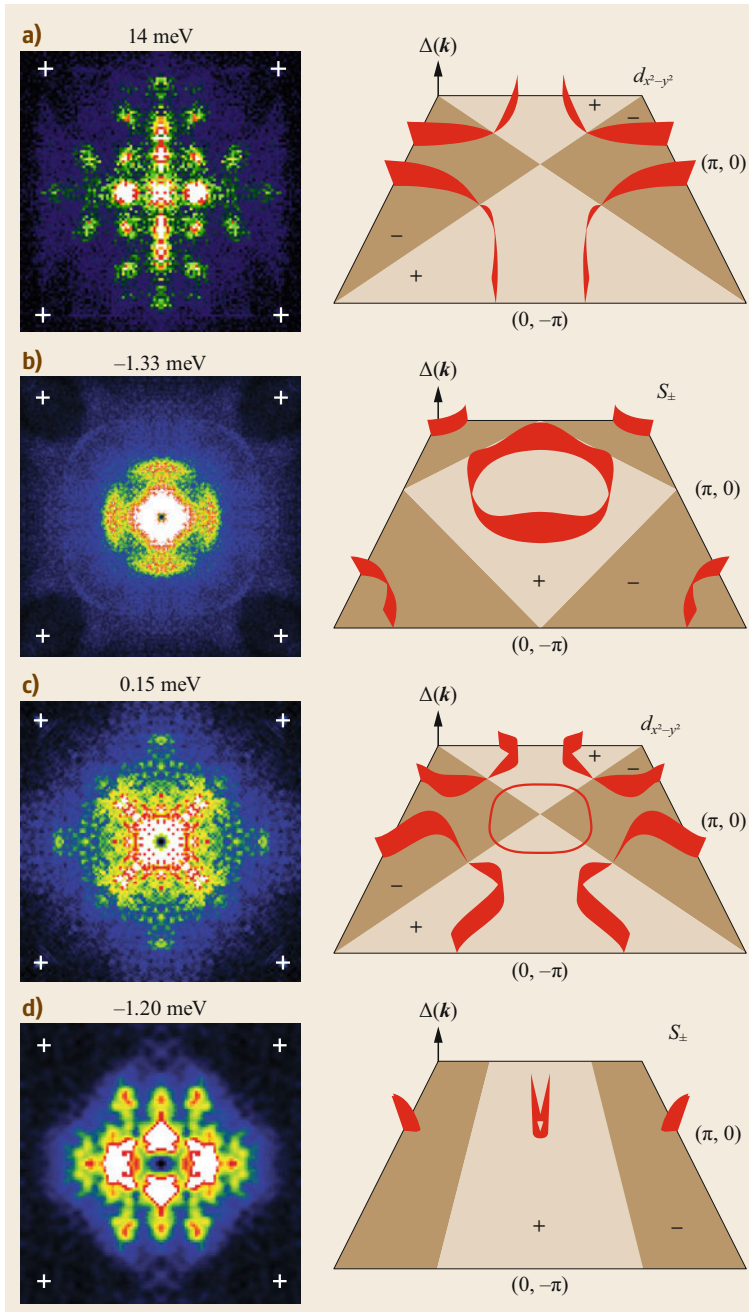

Fig. 28.6 (a) *Left*: Bogoliubov quasiparticle interference (BQPI) patterns $g(\mathbf{q}, E)$ within $E < \Delta(\mathbf{k})^{\max}$ in $Bi_2Sr_2CaCu_2O_8$; *right*: resulting measured $\Delta_{SC}(\mathbf{k})$. (b) *Left*: BQPI patterns $g(\mathbf{q}, E)$ within $E < \Delta(\mathbf{k})^{\max}$ in LiFeAs; *right*: resulting measured $\Delta_{SC}(\mathbf{k})$. (c) *Left*: BQPI patterns $g(\mathbf{q}, E)$ within $E < \Delta_{\mathbf{k}}^{\max}$ in CeCoIn$_5$; *right*: resulting measured $\Delta_{SC}(\mathbf{k})$. From [28.52]. (d) *Left*: BQPI patterns $g(\mathbf{q}, E)$ within $E < \Delta(\mathbf{k})^{\max}$ in FeSe for α-band; *right*: resulting measured $\Delta_{SC}(\mathbf{k})$. From [28.54]. Reprinted with permission from AAAS

Determination of $\Delta(\mathbf{k})$ in iron pnictides e.g., LiFeAs is somewhat similar but complicated by the multiple bands. Given the tetragonal crystal symmetry, four minima in the $\Delta_i(\mathbf{k})$ for three bands $i = 1, 2, 3$ are consistent with the observed triple set of dispersive $\mathbf{q}_j(E)$ maxima (Fig. 28.6b, *left*). Inverting sets of $\mathbf{q}_j(E)$ in the energy-range $\Delta(\mathbf{k})^{\mathrm{min}} < E < \Delta(\mathbf{k})^{\mathrm{max}}$, gives the gap structure shown in Fig. 28.6b (*right*) [28.65]. At present, we do not have a direct measure of the sign change between bands.

Determination of $\Delta(\mathbf{k})$ in heavy-fermion superconductors e.g., CeCoIn$_5$ is based on the dispersive $\delta N(\mathbf{q}, E) \propto \delta g(\mathbf{q}, E)$ modulations at wavevectors $\mathbf{q}_j(E)$ as shown in Fig. 28.6c (*left*). Given the tetragonal nature of the crystal and even though there are two heavy bands, four zeros in the $\Delta(\mathbf{k})$ along the $(\pm 1, \pm 1)$ di-

rections are consistent with the observed *octet* of $\mathbf{q}_j(E)$ maxima. Inverting set $\mathbf{q}_j(E)$ in the energy-range $0 < E < \Delta(\mathbf{k})^{\mathrm{max}}$ gives the gap structure shown in Fig. 28.6c (*right*) [28.52].

Determination of $\Delta(\mathbf{k})$ in iron chalcogenides e.g., FeSe is complicated by the strongly nematic electronic structure. Nevertheless, for FeSe the dispersive $\delta N(\mathbf{q}, E) \propto \delta g(\mathbf{q}, E)$ modulations at wavevectors $\mathbf{q}_j(E)$ are as shown in Fig. 28.6d (*left*). Given the orthorhombic nature of the crystal, a gap structure with two minima in each of the $\Delta_i(\mathbf{k})$ for $i = 1, 2$, provides an excellent consistency with the data. Moreover, phase-resolved determination of sign-changing energy gaps $\Delta(\mathbf{k})$ on different bands is possible here so that the $\Delta_i(\mathbf{k})$ are as shown in Fig. 28.6d (*right*) [28.54].

28.9 Real–Space Imaging of Energy Gaps of Ordered Phases

When the $\mathbf{k}$-space energy-gap $\Delta(\mathbf{k})$ of an ordered state exists, it produces a strong impact on $N(\mathbf{r}, E)$. In a homogeneous system, this occurs simply: within the energy-range $|E| < \Delta$ where fewer (or no) quasiparticle eigenstates $\psi_\mathbf{k}(E)$ exist, $N(E)$ is strongly suppressed. This is referred to colloquially as the *tunneling* energy gap because it is detectable in planar tunnel junctions. When strong interactions occur between the electrons of this ordered state and impurity/dopant atoms, the electron–electron interactions that produce the energy gap are altered locally, with a resulting spatial variation in the tunneling gap $\Delta(\mathbf{r})$. Modern SI-STM allows atomically resolved visualization of $\Delta(\mathbf{r})$ in a process referred to as a "gapmap" [28.66] and, more importantly, it is possible to simultaneously determine where the dopant/impurity atoms reside in the crystal and so to find their effect directly at atomic scale. Below we discuss several examples of this key procedure.

Cu-based high-temperature superconductivity is often achieved by inserting O^{2-} ions into interstitial sites in the cuprate crystal. Imaging the random distribution of dopant O^{2-} ions can be achieved (Fig. 28.7a, *left*) by detecting the doubly charged state as an atomic scale peak in tunnel conductance far below E_F. The atomic-scale electronic structure is imaged simultaneously using $g(\mathbf{r}, E)$, and the magnitude of the energy-gap $\Delta(\mathbf{r})$ identified as half the energy range within which there is strong suppression in $g(\mathbf{r}, E)$ is de-

termined [28.67] (Fig. 28.7a, *right*). Correspondence between the dopant-ion map and the gapmap reveal the ions as a primary cause of the intense nanoscale electronic disorder [28.68, 69].

Fe-based is, likewise, often achieved by inserting substitution atoms on the Fe site e.g., Cr or on the pnictide/chalcogenide site e.g., P for As or Te for Se. Thus for example, imaging distribution of dopant Te atoms in FeSeTe can be achieved (Fig. 28.7b, *left*). The simultaneous atomic-scale image of energy-gap $\Delta(\mathbf{r})$ shows some but not dominant disorder in these materials (Fig. 28.7b, *right*).

Ferromagnetic topological insulators (FMTI) have been created by substituting Cr ions on the Bi/Sb site in $Cr_x(Bi_{0.1}Sb_{0.9})_{2-x}Te_3$ for example. By imaging the random locations of each magnetic Cr dopant atom (Fig. 28.7c, *left*) simultaneously with the magnitude of the Dirac-mass gapmap $\Delta_{\mathrm{FM}}(\mathbf{r})$, intense Dirac-mass disorder is observed (Fig. 28.7c, *right*) and is traced directly to the Cr distribution [28.57].

Spinless Th atoms substituted at the U sites in the heavy-fermion compound URu$_2$Si$_2$ are distributed sparsely but randomly (Fig. 28.7d, *left*). Simultaneous visualization of the hybridization gapmap $\Delta_{\mathrm{HF}}(\mathbf{r})$ (Fig. 28.7d, *right*) allows one to demonstrate that the Th atoms generate the nanoscale hybridization disorder expected of spinless *Kondo-holes* in any HF material [28.70].
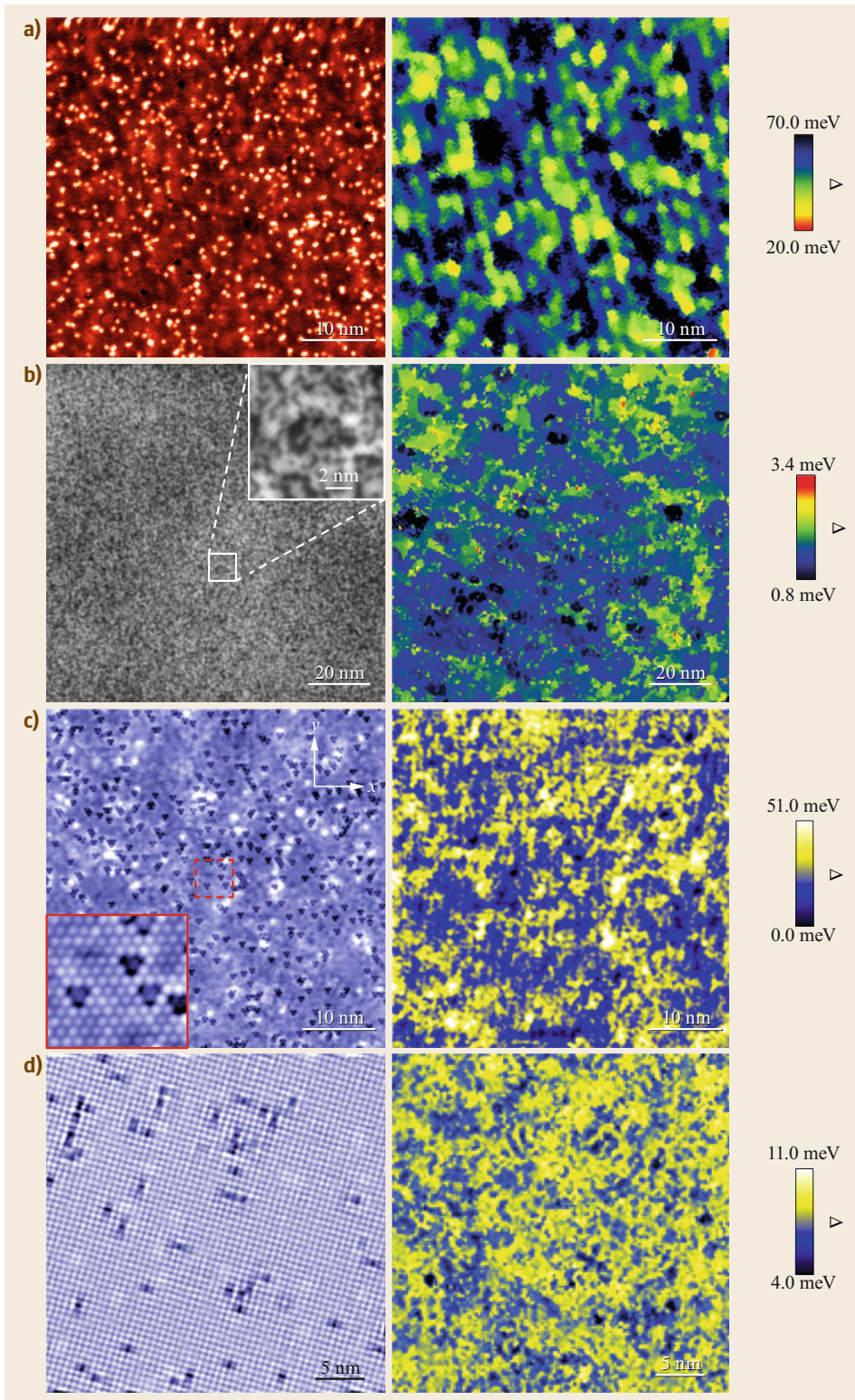
Fig. 28.7 **(a)** *Left panel* shows image of locations of individual O^{2-} dopant ions in $Bi_2Sr_2CaCu_2O_8$ and *right panel* shows the simultaneously measured but microscopically unidentified energy gap of $\Delta(\boldsymbol{r})$. From [28.67]. Reprinted with permission from AAAS. **(b)** *Left panel* shows topographic image of FeSeTe revealing the substitutional sites of Te for Se, and *right panel* shows the simultaneously measured Cooper-pairing energy gap of $\Delta_{SC}(\boldsymbol{r})$. **(c)** *Left panel* shows image of locations of individual Cr atoms substituted at the Bi/Sb sites in $Cr_x(Bi_{0.1}Sb_{0.9})_{2-x}Te_3$, and *right panel* shows the simultaneously measured Dirac-mass gap $\Delta_{FM}(\boldsymbol{r})$. From [28.56]. **(d)** *Left panel* shows image of locations of individual Th atoms substituted at the U sites in URu_2Si_2, and *right panel* shows the simultaneously measured URu_2Si_2 hybridization energy gap of $\Delta_{HF}(\boldsymbol{r})$. From [28.70]

28.10 Visualizing Electronic Symmetry Breaking

When EQM undergoes a phase transition to a state with symmetry that is lower than the point-group symmetry of the crystal, spontaneous electronic symmetry breaking is said to occur. Fourier analysis of SI-STM images $T(\boldsymbol{r}, V_{\mathrm{S}})$ and $g(\mathbf{r}, V)$ to yield

$$T(\boldsymbol{q}, V_{\mathrm{S}}) = \Re e\left\{T(\boldsymbol{q}, V_{\mathrm{S}})\right\} + i\Im m\left\{T(\boldsymbol{q}, V_{\mathrm{S}})\right\}$$

and

$$g(\boldsymbol{q}, V) = \Re e\left\{g(\boldsymbol{q}, V)\right\} + i\Im m\left\{g(\boldsymbol{q}, V)\right\}$$

is then a powerful technique to determine which symmetries are broken. Below we discuss the approaches used for detection of rotational, inversion, and various types of translational symmetry breaking.

An electronic nematic phase is an EQM state that breaks rotational symmetry globally or at $Q = 0$. In fact, for this to occur the electronic structure inside each crystal unit cell must exhibit lower symmetry than that cell. To detect this effect in SI-STM one focuses on the Bragg wavevectors which, for example in a tetragonal crystal, would be labeled $\boldsymbol{Q}_x^B$ and $\boldsymbol{Q}_y^B$. The real components $\Re e\{g(\boldsymbol{Q}_x^B, E)\}$; $\Re e\{g(\boldsymbol{Q}_y^B, E)\}$ (or perhaps $\Re e\{T(\boldsymbol{Q}_x^B, V)\}$; $\Re e\{T(\boldsymbol{Q}_y^B, V)\}$) of the Bragg amplitudes of $g(\boldsymbol{q}, E)$ provide a direct measure of intraunit-cell nematicity

$$N(E) \equiv \Re e\left\{g(\boldsymbol{Q}_y^B, E)\right\} - \Re e\left\{g(\boldsymbol{Q}_x^B, E)\right\}. \quad (28.17)$$

In general, if the $N(E)$ is nonzero, breaking of intraunit-cell C_4-symmetry is occurring and the electronic structure is nematic.

To detect inversion breaking at $Q = 0$ in SI-STM data, one again focuses on the Bragg wavevectors $\boldsymbol{Q}_x^B$ and $\boldsymbol{Q}_y^B$ but now with the imaginary components $\Im m\left\{g(\boldsymbol{Q}_x^B, E)\right\}$; $\Im m\left\{g(\boldsymbol{Q}_y^B, E)\right\}$ of the Bragg amplitudes of $g(\boldsymbol{q}, E)$. A direct measure of intraunit-cell inversion breaking is

$$I(E) \equiv \Im m\left\{g(\boldsymbol{Q}_y^B, E)\right\} + \Im m\left\{g(\boldsymbol{Q}_x^B, E)\right\}. \quad (28.18)$$

In general, if the $I(E)$ is nonzero, intraunit-cell inversion-symmetry breaking is occurring.

Translational symmetry breaking at $\boldsymbol{Q} \neq 0$ in SI-STM data occurs if there are any periodic modulations of electronic structure whose wavevectors $\boldsymbol{Q}$ are not at any of the Bragg wavevectors of the crystal. Such a modulation can be described by $A(r) = AF(\theta)\cos(\boldsymbol{Q} \cdot \boldsymbol{r} + \phi(\boldsymbol{r}))$ where $A(\boldsymbol{r})$ represents the modulating electronic degree of freedom with amplitude A, $\boldsymbol{Q}$ is the

wavevector, and $F(\theta)$ is the modulation form factor. For a tetragonal crystal, an s-symmetry form factor $F_s(\theta)$ is even under $90°$ rotations whereas a d-wave form factor is $F_d(\theta)$ is odd. To show the existence of translational symmetry breaking usually only requires detection of one or more nondispersive maxima in $g(\boldsymbol{q}, V)$ at some incommensurate $\boldsymbol{Q}$ within the first Brillouin zone. To understand and identify the modulating state is more challenging, however, because of the form factor $F(\theta)$.

For that, sublattice-phase-resolved $g(\boldsymbol{r}, E)$ images are required. As an example of this procedure we consider the CuO_2 unit cell in the superconducting plane of cuprates. The $g(\boldsymbol{r}, E)$ data, measured with many pixels within each unit cell, is separated into three: $Cu(\boldsymbol{r})$, containing only Cu sites and, $O_x(\boldsymbol{r})$; $O_y(\boldsymbol{r})$, containing only the x/y-axis oxygen sites. Phase-resolved Fourier transforms of the $O_x(\boldsymbol{r})$ and $O_y(\boldsymbol{r})$ sublattice images $\tilde{O}_x(\boldsymbol{q}) = \Re e\left\{\tilde{O}_x(\boldsymbol{q})\right\} + i\Im m\left\{\tilde{O}_x(\boldsymbol{q})\right\}$; $\tilde{O}_y(\boldsymbol{q}) = \Re e\left\{\tilde{O}_y(\boldsymbol{q})\right\} + i\Im m\left\{\tilde{O}_y(\boldsymbol{q})\right\}$, are used to determine the form factor symmetry for modulations at any $\boldsymbol{q}$

$$D(\boldsymbol{q}) = [\tilde{O}_x(\boldsymbol{q}) - \tilde{O}_y(\boldsymbol{q})]/2 \,, \quad (28.19a)$$
$$S'(\boldsymbol{q}) = [\tilde{O}_x(\boldsymbol{q}) + \tilde{O}_y(\boldsymbol{q})]/2 \,, \quad (28.19b)$$
$$S(\boldsymbol{q}) = \widetilde{Cu}(\boldsymbol{q}) \,. \quad (28.19c)$$

Specifically, for a modulation occurring at $\boldsymbol{Q}$, one can evaluate the magnitude of its d-symmetry form factor $\tilde{D}(\boldsymbol{Q})$ and its s'- and s-symmetry form factors $\tilde{S}'(\boldsymbol{Q})$ and $\tilde{S}(\boldsymbol{Q})$, respectively. Figure 28.8b shows $D(\boldsymbol{q}, 94\,\mathrm{meV})$ derived from $g(\boldsymbol{r}, V = 94\,\mathrm{meV})$ in Fig. 28.8a.

Finally, to determining the amplitude and phase of modulations at a given Q, inverse Fourier filtering of $A(\boldsymbol{q}) \equiv D(\boldsymbol{q})$ or of $A(\boldsymbol{q}) \equiv S'(\boldsymbol{q})$ or of $A(\boldsymbol{q}) \equiv S(\boldsymbol{q})$ can be carried out for any form factor. For example, suppose the modulation occur at two orthogonal wavevectors $\boldsymbol{Q}_x$; $\boldsymbol{Q}_y$, Fourier filtering only those regions surrounding $\boldsymbol{Q}_x$ and $\boldsymbol{Q}_y$ generates two complex-valued $\boldsymbol{r}$-space images $A_x(\boldsymbol{r}), A_y(\boldsymbol{r})$

$$A_x(\boldsymbol{r}) = \frac{2}{(2\pi)^2} \int d\boldsymbol{q} e^{i\boldsymbol{q}\cdot\boldsymbol{r}} e^{i\boldsymbol{Q}_x\cdot\boldsymbol{r}} A(\boldsymbol{q}) e^{-\frac{(\boldsymbol{q})^2}{2\Lambda^2}} \,,$$
$$A_y(\boldsymbol{r}) = \frac{2}{(2\pi)^2} \int d\boldsymbol{q} e^{i\boldsymbol{q}\cdot\boldsymbol{r}} e^{i\boldsymbol{Q}_y\cdot\boldsymbol{r}} A(\boldsymbol{q}) e^{-\frac{(\boldsymbol{q})^2}{2\Lambda^2}} \,, \quad (28.20a)$$

where Λ^{-1} is the characteristic length scale over which variations in $A_x(\boldsymbol{r})$, $A_y(\boldsymbol{r})$ can be resolved, and is set by the filter width in Fourier space. Figure 28.8c shows a typical example of $A_y(\boldsymbol{r})$ determined at $\boldsymbol{Q}_y$ of Fig. 28.8b, in this fashion. Equivalently, the spatial-
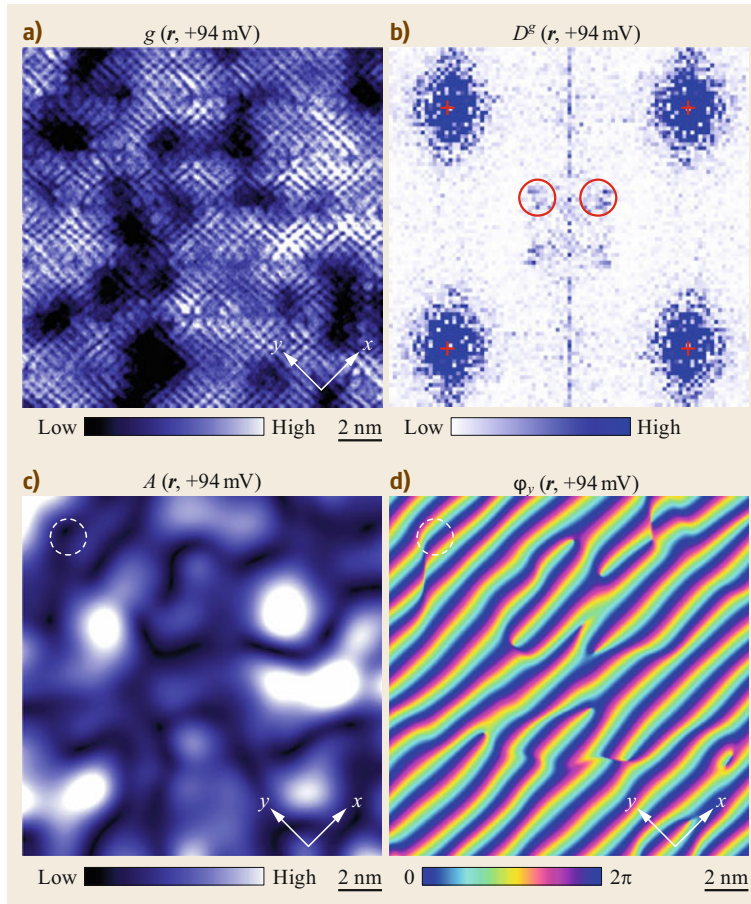
Fig. 28.8 (a) Measured $g(\boldsymbol{q}, E) \propto N(\boldsymbol{q}, E)$ image of disordered density wave (DW) state in $Bi_2Sr_2CaCu_2O_8$. **(b)** $D^g(\boldsymbol{q}, E = 94\,\mathrm{meV})$ is the d-symmetry form factor Fourier transform of A showing that the DW modulations at Q_x; Q_y have predominantly d-symmetry. **(c)** Measured $A(\boldsymbol{r})$ for the d-symmetry form factor modulations at $\boldsymbol{Q}_y$ in **(a,b)**. **(d)** Spatial-phase $\phi(\boldsymbol{r})$ of d-symmetry form factor modulations at $\boldsymbol{Q}_y$ in **(a,b)**. From [28.34]

phase information of a given modulation can be visualized as

$$\phi_x(\boldsymbol{r}) = \arctan\left(\frac{\mathfrak{Im}\{A_x(\boldsymbol{r})\}}{\mathfrak{Re}\{A_x(\boldsymbol{r})\}}\right),$$

$$\phi_y(\boldsymbol{r}) = \arctan\left(\frac{\mathfrak{Im}\{A_y(\boldsymbol{r})\}}{\mathfrak{Re}\{A_y(\boldsymbol{r})\}}\right). \tag{28.20b}$$

Figure 28.8d shows a typical example of $\phi_y(\boldsymbol{r})$ determined at $\boldsymbol{Q}_y$ of Fig. 28.9b, in this fashion.

28.11 Visualizing New Phases of Strong–Correlation Electronic Matter

In this last section, we give some specific examples of how the SI-STM techniques for detection of electronic symmetry breaking introduced above can be used to search for novel phases of strong-correlation electronic matter.

To detect and visualize an electronic nematic phase in Cu-based high-temperature superconductors, $g(\boldsymbol{r}, E)$ data with up to 49 pixels inside the CuO_2 unit cell are used. Figure 28.9a is typical of $Bi_2Sr_2CaCu_2O_8$, with O sites indicated by dashes. Taking the phase-resolved Fourier transform $g(\boldsymbol{q}, V) = \mathfrak{Re}\{g(\boldsymbol{q}, V)\} + i\mathfrak{Im}\{g(\boldsymbol{q}, V)\}$ and then applying (28.17) for comparison of intensities at the two Bragg peaks, the intraunit-cell rotational symmetry breaking is detected as shown in the inset [28.66, 71].

Similarly, for the electronic nematic phase in Fe-based high-temperature superconductors, $g(\boldsymbol{r}, E)$ data with up to 49 pixels inside the Fe–Fe unit cell are used. Figure 28.9b is typical of FeSe with Fe sites indicated by dots. Taking $g(\boldsymbol{q}, V) = \mathfrak{Re}\{g(\boldsymbol{q}, V)\} +$
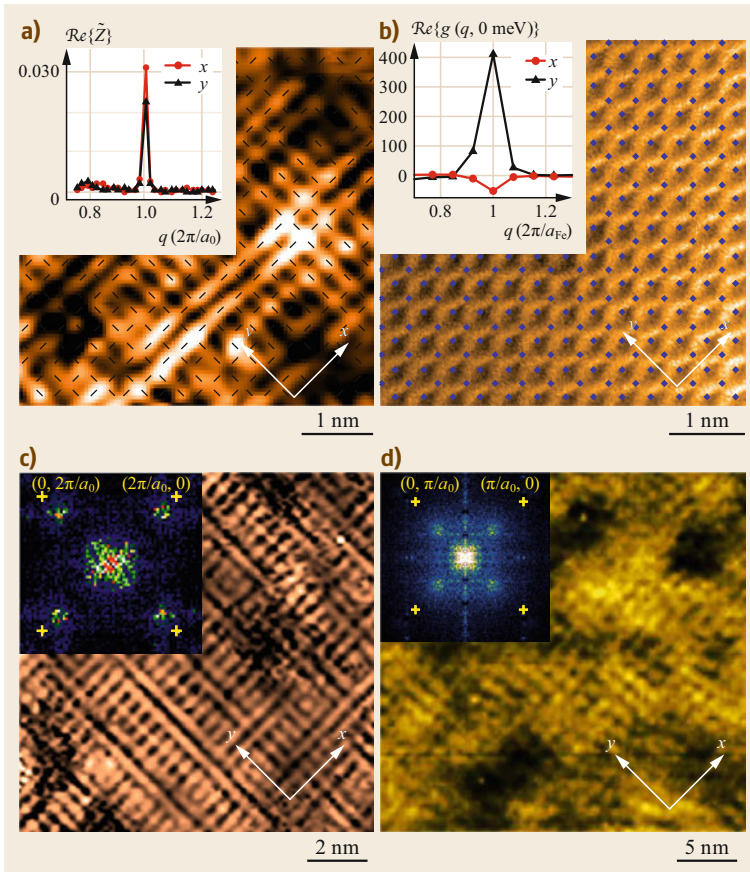
Fig. 28.9 (**a**) Measured $g(\boldsymbol{r}, E)$ of underdoped $Bi_2Sr_2CaCu_2O_8$, with O sites indicated by *dashes*. *Inset* shows intensities at the two phase-resolved Bragg peaks revealing intraunit-cell rotational symmetry breaking. (**b**) Measured $g(\boldsymbol{r}, E)$ of FeSe, with Fe sites indicated by dots. *Inset* shows intensities at the two phase-resolved Bragg peaks revealing intraunit-cell rotational symmetry breaking. (**c**) Measured $g(\boldsymbol{r}, E)$ of DW state of $Ca_{2-x}Na_xCuO_2Cl_2$. *Inset* shows Fourier transform. (**d**) Nanometer-resolution SJTM image of the Cooper-pair condensate in $Bi_2Sr_2CaCu_2O_8$. *Inset* is its s-symmetry Fourier transform showing that a Cooper-pair density wave exists in cuprates

$i\mathfrak{Im}\{g(\boldsymbol{q}, V)\}$ and then applying (28.17) for comparison of intensities specifically between the two Bragg peaks of the Fe sublattice, the intraunit-cell rotational symmetry breaking of Fe-based compounds [28.72] is detected as shown in the inset.

To detect and visualize a translational symmetry breaking in EQM in Cu-based high-temperature superconductors, $g(\boldsymbol{r}, E)$ data as in Fig. 28.9c from $Ca_{2-x}Na_xCuO_2Cl_2$ are used. Inset shows the d-symmetry Fourier transform (28.19a) of Fig. 28.9c with the two incommensurate peaks at $\boldsymbol{Q}_x$, $\boldsymbol{Q}_y$ clearly visible [28.73, 74]. This state certainly has a d-symmetry form factor and is widely referred to as a *charge* density wave (CDW) because charge modulations occur. But, although a necessary condition, such charge modulations are not a sufficient condition to identify the state and it could also be a PDW state.

To detect and visualize a PDW state, a scanned Josephson tunneling microscope operating at millikelvin temperatures is used to determine the Josephson (pair tunneling) critical current $I_C(\boldsymbol{r})$ at every pixel. Figure 28.9d is a typical SJTM image of the Cooper-pair condensate in $Bi_2Sr_2CaCu_2O_8$ achieved in this

fashion. The inset is its s-symmetry Fourier transform showing that a Cooper-pair density wave exists in cuprates [28.36].

References

28.1   K. Yosida: *Theory of Magnetism* (Springer, Berlin, Heidelberg 1996)

28.2   J.R. Schrieffer: *Theory of Superconductivity* (Perseus, New York 1991)

28.3   G. Grüner: *Density Waves in Solids* (Addison-Wesley, Boston 1989)

28.4   N.W. Ashcroft, N.D. Mermin: *Solid State Physics* (Brooks Cole, Boston 1976)

28.5   A.C. Hewson: *The Kondo Problem to Heavy Fermions* (Cambridge Univ. Press, Cambridge 1993)

28.6   A.J. Schofield: Non-Fermi liquids, Contemp. Phys. **40**, 95–115 (1999)

28.7   P. Coleman: *Handbook of Magnetism and Advanced Magnetic Materials*, Vol. 1 (Wiley, Hoboken 2007)

28.8   J. Kondo: Resistance minimum in dilute magnetic alloys, Prog. Theor. Phys. **32**, 37–49 (1964)

28.9   G.R. Stewart: Heavy-fermion systems, Rev. Mod. Phys. **56**, 755–787 (1984)

28.10   F. Steglich: Superconductivity and magnetism in heavy-fermion compounds, J. Phys. Soc. Jpn. **74**, 167–177 (2005)

28.11   P. Fulde, J. Keller, G. Zwicknagl: Theory of heavy fermion systems, Solid State Phys. **41**, 1–151 (1988)

28.12   N.F. Mott: The basis of the electron theory of metals, with special reference to the transition metals, Proc. Phys. Soc. A **62**, 416 (1949)

28.13   A. Georges, L. de' Medici, J. Mravlje: Strong correlations from Hund's coupling, Annu. Rev. Condens. Matter Phys. **4**, 137–178 (2013)

28.14   L. de' Medici, S.R. Hassan, M. Capone, X. Dai: Orbital-selective Mott transition out of band degeneracy lifting, Phys. Rev. Lett. **102**, 126401 (2009)

28.15   E. Jakobi, N. Blüme, P. van Dongen: Orbital-selective Mott transitions in a doped two-band Hubbard model, Phys. Rev. B **80**, 115109 (2009)

28.16   L. de' Medici, J. Mravlje, A. Georges: Janus-faced influence of Hund's rule coupling in strongly correlated materials, Phys. Rev. Lett. **107**, 256401 (2011)

28.17   L. Balents: Spin liquids in frustrated magnets, Nature **464**, 199 (2010)

28.18   P.A. Lee, N. Nagaos, X.-G. Wen: Doping a Mott insulator: Physics of high-temperature superconductivity, Rev. Mod. Phys. **78**, 17 (2006)

28.19   E. Dagotto: Correlated electrons in high-temperature superconductors, Rev. Mod. Phys. **66**, 763 (1994)

28.20   A. Georges, G. Kotliar, W. Krauth, M.J. Rozenberg: Dynamical mean-field theory of strongly correlated fermion systems and the limit of infinite dimensions, Rev. Mod. Phys. **68**, 13 (1996)

28.21   N. Read, S. Sachdev: Valence-bond and spin-Peierls ground states of low-dimensional quantum antiferromagnets, Phys. Rev. Lett. **62**, 1694 (1989)

28.22   J. Zaanen, O. Gunnarsson: Charged magnetic domain lines and the magnetism of high-T_c oxides, Phys. Rev. B **40**, 7391 (1989)

28.23   S.A. Kivelson, E. Fradkin, V.J. Emery: Electronic liquid-crystal phases of a doped Mott insulator, Nature **393**, 550 (1998)

28.24   V.J. Emery, S.A. Kivelson, J.M. Tranquada: Striped phases in high-temperature superconductors, Proc. Natl. Acad. Sci. USA **96**, 8814 (1999)

28.25   S. Sachdev: Colloquium: Order and quantum phase transitions in the cuprate superconductors, Rev. Mod. Phys. **75**, 913 (2003)

28.26   S.A. Kivelson, E. Fradkin, J. Tranquada: Colloquium: Theory of intertwined orders in high temperature superconductors, Rev. Mod. Phys. **87**, 457 (2015)

28.27   S.H. Pan, E.W. Hudson, J.C. Davis: ^{3}He refrigerator based very low temperature scanning tunneling microscope, Rev. Sci. Instrum. **70**, 1459–1463 (1999)

28.28   K. Fujita, M. Hamidian, I. Firmo, S. Mukhopadhyay, C.K. Kim, H. Eisaki, S. Uchida, J.C. Davis: Spectroscopic imaging STM. In: *Strongly Correlated Systems—Experimental Techniques*, ed. by A. Avella, F. Mancini (Springer, Berlin Heidelberg 2014)

28.29   R.J. Hamers, R.M. Tromp, J.E. Demuth: Surface electronic structure of Si(111)-(7×7) resolved in real space, Phys. Rev. Lett. **56**, 1972 (1986)

28.30   H.L. Edwards, D.J. Derro, A.L. Barr, J.T. Markert, A.L. de Lozanne: Spatially varying energy gap in the CuO chains of $YBa_2Cu_3O_{7-x}$ detected by scanning tunneling spectroscopy, Phys. Rev. Lett. **75**, 1387 (1995)

28.31   M.H. Hamidian, I.A. Firmo, K. Fujita, S. Mukhopadhyay, J.W. Orenstein, H. Eisaki, S. Uchida, M.J. Lawler, E.-A. Kim, J.C. Davis: Picometer registration of zinc impurity states in $Bi_2Sr_2CaCu_2O_{8+\delta}$ for phase determination in intra-unit-cell Fourier transform STM, New J. Phys. **14**, 053017 (2012)

28.32   J.A. Slezak, J. Lee, M. Wang, K. McElroy, K. Fujita, B.M. Anderson, P.J. Hirschfeld, H. Eisaki, S. Uchida, J.C. Davis: Imaging the impact on cuprate superconductivity of varying the interatomic distances within individual crystal unit cells, Proc. Natl. Acad. Sci. USA **105**, 3203–3208 (2008)

28.33   K. Fujita, M.H. Hamidian, S.D. Edkins, C.K. Kim, Y. Kohsaka, M. Azuma, M. Takano, H. Takagi, H. Eisaki, S. Uchida, A. Allais, M.J. Lawler, E.-A. Kim, S. Sachdev, J.C. Séamus Davis: Direct phase-sensitive identification of a d-form factor density wave in underdoped cuprates, Proc. Natl. Acad. Sci. USA **111**(30), E3026–E3032 (2014)

28.34   M.H. Hamidian, S.D. Edkins, C.K. Kim, J.C. Séamus Davis, A.P. Mackenzie, H. Eisaki, S. Uchida, M.J. Lawler, E.-A. Kim, S. Sachdev, K. Fujita: Atomic-scale electronic structure of the cuprate d-symmetry form factor density wave state, Nat. Phys. **12**(2), 150–156 (2016)

28.35   P.M. Chaikin, T.C. Lubensky: *Principles of Condensed Matter Physics* (Cambridge Univ. Press, Cambridge 2010)

28.36   M. Hamidian, S.D. Edkins, S.H. Joo, A. Kostin, H. Eisaki, S. Uchida, M.J. Lawler, E.-A. Kim, A.P. MacKenzie, K. Fujita, J. Lee, J.C. Séamus

Davis: Detection of a Cooper-pair density wave in $Bi_2Sr_2CaCu_2O_{8+x}$, Nature **532**, 343 (2016)

28.37 J. Šmakov, I. Martin, A.V. Balatsky: Josephson scanning tunneling microscopy, Phys. Rev. B **64**, 212506 (2001)

28.38 O. Naaman, W. Teizer, R.C. Dynes: Flucuation dominated Josephson tunneling with a scanning tunneling microscope, Phys. Rev. Lett. **87**, 097004 (2001)

28.39 J.G. Rodrigo, H. Suderow, S. Vieria: On the use of STM superconducting tips at very low temperatures, Eur. Phys. J. **40**, 483 (2004)

28.40 T. Proslier, A. Kohen, Y. Noat, T. Cren, D. Roditchev, W. Sacks: Probing the superconducting condensate on a nanometer scale, Europhys. Lett. **73**, 962 (2006)

28.41 H. Kimura, R.P. Barber Jr., S. Ono, Y. Ando, R.C. Dynes: Scanning Josephson tunneling microscopy of single-crystal $Bi_2Sr_2CaCu_2O_{8+\delta}$ with a conventional superconducting tip, Phys. Rev. Lett. **101**, 037002 (2008)

28.42 M.F. Crommie, C.P. Lutz, D.M. Eigler: Imaging standing waves in a two-dimensional electron gas, Nature **363**, 524–527 (1993)

28.43 A. Yazdani, B.A. Jones, C.P. Lutz, D.M. Eigler: Probing the local effects of magnetic impurities on superconductivity, Science **275**, 1767–1770 (1997)

28.44 A.V. Balatsky, I. Vekhter, J.-X. Zhu: Impurity-induced states in conventional and unconventional superconductors, Rev. Mod. Phys. **78**, 373 (2006)

28.45 S.H. Pan, E.W. Hudson, K.M. Lang, H. Eisaki, S. Uchida, J.C. Davis: Imaging the effects of individual zinc impurity atoms on superconductivity in $Bi_2Sr_2CaCu_2O_{8+\delta}$, Nature **403**, 746 (2000)

28.46 E.W. Hudson, K.M. Lang, V. Madhavan, S.H. Pan, H. Eisaki, S. Uchida, J.C. Davis: Interplay of magnetism and high-T_c superconductivity at individual Ni impurity atoms in $Bi_2Sr_2CaCu_2O_{8+\delta}$, Nature **411**, 920 (2001)

28.47 Q.-H. Wang, D.-H. Lee: Quasiparticle scattering interference in high-temperature superconductors, Phys. Rev. B **67**(R), 020511 (2003)

28.48 L. Capriotti, D.J. Scalapino, R.D. Sedgewick: Wave-vector power spectrum of the local tunneling density of states, Phys. Rev. B **68**, 014508 (2003)

28.49 T. Yuan, J. Figgins, D.K. Morr: Hidden order transition in URu_2Si_2: Evidence for the emergence of a coherent Anderson lattice from scanning tunneling spectroscopy, Phys. Rev. B **86**, 035129 (2012)

28.50 J. Lee, M.P. Allan, M.A. Wang, J. Farrell, S.A. Grigera, F. Baumberger, J.C. Davis, A.P. Mackenzie: Heavy d-electron quasiparticle interference and real-space electronic structure of $Sr_3Ru_2O_7$, Nat. Phys. **5**, 800–804 (2009)

28.51 A.R. Schmidt, M.H. Hamidian, P. Wahl, F. Meier, A.V. Balatsky, J.D. Garrett, T.J. Williams, G.M. Luke, J.C. Davis: Imaging the Fano lattice to 'hidden order' transition in URu_2Si_2, Nature **465**, 570–576 (2010)

28.52 M.P. Allan, F. Massee, D.K. Morr, J. van Dyke, A.W. Rost, A.P. Mackenzie, C. Petrovic, J.C. Davis: Imaging cooper pairing of heavy fermions in $CeCoIn_5$, Nat. Phys. **9**, 468–473 (2013)

28.53 H. Pirie, J.E. Hoffman, Y. He, M.M. Yee, A. Soumyanarayanan, D.-J. Kim, Z. Fisk, D. Morr, M.H. Hamidian: Visualizing the topologically induced states of strongly correlated electrons in SmB_6, Bull. Am. Phys. Soc. **62**, MARS37010P (2017)

28.54 P.O. Sprau, A. Kostin, A. Kreisel, A.E. Böhmer, V. Taufour, P.C. Canfield, S. Mukherjee, P.J. Hirschfeld, B.M. Andersen, J.C. Séamus Davis: Discovery of orbital-selective Cooper pairing in FeSe, Science **357**, 75 (2017)

28.55 M.Z. Hasan, C.L. Kane: Colloquium: Topological insulators, Rev. Mod. Phys. **82**, 3045 (2010)

28.56 I. Lee, C.K. Kim, J. Lee, S.J.L. Billinge, R. Zhong, J.A. Schneeloch, T. Liu, T. Valla, J.M. Tranquada, G. Gu, J.C. Séamus Davis: Imaging Dirac-mass disorder from magnetic dopant atoms in the ferromagnetic topological insulator $Cr_x(Bi_{0.1}Sb_{0.9})_{2-x}Te_3$, Proc. Natl. Acad. Sci. USA **112**, 1316 (2015)

28.57 A. Georges, L. de' Medici, J. Mravlje: Strong correlations from Hund's coupling, Annu. Rev. Condens. Matter Phys. **4**, 137–178 (2013)

28.58 E. Pavarini: Hund's metals: Explained. In: *The Physics of Correlated Insulators, Metals, and Superconductors Modeling and Simulation*, Vol. 7, ed. by E. Koch, R. Scalettar, R. Martin (Forschungszentrum Jülich, Jülich 2017)

28.59 Z.P. Yin, K. Haule, G. Kotliar: Kinetic frustration and the nature of the magnetic and paramagnetic states in iron pnictides and iron chalcogenides, Nat. Mater. **10**, 932–935 (2011)

28.60 J.E. Hoffman, K. McElroy, D.-H. Lee, K.M. Lang, H. Eisaki, S. Uchida, J.C. Davis: Imaging quasiparticle interference in $Bi_2Sr_2CaCu_2O_{8+\delta}$, Science **297**, 1148 (2002)

28.61 K. McElroy, R.W. Simmonds, J.E. Hoffman, D.-H. Lee, J. Orenstein, H. Eisaki, S. Uchida, J.C. Davis: Relating atomic-scale electronic phenomena to wave-like quasiparticle states in superconducting $Bi_2Sr_2CaCu_2O_{8+\delta}$, Nature **422**, 592 (2003)

28.62 T. Hanaguri, C. Lupien, Y. Kohsaka, D.-H. Lee, M. Azuma, M. Takano, H. Takagi, J.C. Davis: A 'checkerboard' electronic crystal state in lightly hole-doped $Ca_{2-x}Na_xCuO_2Cl_2$, Nature **430**, 1001 (2004)

28.63 Y. Kohsaka, C. Taylor, P. Wahl, A. Schmidt, J. Lee, K. Fujita, J.W. Alldredge, K. McElroy, J. Lee, H. Eisaki, S. Uchida, D.-H. Lee, J.C. Davis: How Cooper pairs vanish approaching the Mott insulator in $Bi_2Sr_2CaCu_2O_{8+\delta}$, Nature **454**, 1072 (2008)

28.64 J. Lee, K. Fujita, A.R. Schmidt, C.K. Kim, H. Eisaki, S. Uchida, J.C. Davis: Spectroscopic fingerprint of phase-incoherent superconductivity in the cuprate pseudogap state, Science **325**, 1099 (2009)

28.65 M.P. Allan, A.W. Rost, A.P. Mackenzie, Y. Xie, J.C. Davis, K. Kihou, C.H. Lee, A. Iyo, H. Eisaki, T.-M. Chuang: Anisotropic energy gaps of iron-based superconductivity from intra-band quasiparticle interference in LiFeAs, Science **336**, 563 (2012)

28.66   M.J. Lawler, K. Fujita, J. Lee, A.R. Schmidt, Y. Kohsaka, C.K. Kim, H. Eisaki, S. Uchida, J.C. Davis, J.P. Sethna, E.-A. Kim: Intra-unit-cell electronic nematicity of the high-T_c copper-oxide pseudogap states, Nature **466**, 374 (2010)

28.67   K. McElroy, J. Lee, J.A. Slezak, D.-H. Lee, H. Eisaki, S. Uchida, J.C. Davis: Atomic-scale sources and mechanisms of electronic disorder in $Bi_2Sr_2CaCu_2O_{8+\delta}$, Science **309**, 1048 (2005)

28.68   S.H. Pan, J.P. O'Neal, R.L. Badzey, C. Chamon, H. Ding, J.R. Engelbrecht, Z. Wang, H. Eisaki, S. Uchida, A.K. Gupta, K.-W. Ng, E.W. Hudson, K.M. Lang, J.C. Daivs: Microscopic electronic inhomogeneity in the high-T_c superconductor $Bi_2Sr_2CaCu_2O_{8+x}$, Nature **413**, 282 (2001)

28.69   K.M. Lang, V. Madhavan, J.E. Hoffman, E.W. Hudson, H. Eisaki, S. Uchida, J.C. Davis: Imaging the granular structure of high-T_c superconductivity in underdoped $Bi_2Sr_2CaCu_2O_{8+\delta}$, Nature **415**, 412 (2002)

28.70   M.H. Hamidian, A.R. Schmidt, I.A. Firmo, M.P. Allan, P. Bradley, J.D. Garrett, T.J. Williams, G.M. Luke, Y. Dubi, A.V. Balatsky, J.C. Davis: How Kondo-holes create intense nanoscale heavy-fermion hybrid-ization disorder, Proc. Natl. Acad. Sci. USA **108**, 18233 (2011)

28.71   A. Mesaros, K. Fujita, H. Eisaki, S. Uchida, J.C. Davis, S. Sachdev, J. Zaanen, M.J. Lawler, E.-A. Kim: Topological defects coupling smectic modulations to intra-unit-cell nematicity in cuprates, Science **333**, 426 (2011)

28.72   T.-M. Chuang, M.P. Allan, J. Lee, Y. Xie, N. Ni, S.L. Bud'ko, G.S. Boebinger, P.C. Canfield, J.C. Davis: Nematic electronic structure in the iron-based superconductor $Ca(Fe_{1-x}Co_x)_2As_2$, Science **327**, 181 (2010)

28.73   J.E. Hoffman, E.W. Hudson, K.M. Lang, V. Madhavan, H. Eisaki, S. Uchida, J.C. Davis: A four unit cell periodic pattern of quasi-particle states surrounding vortex cores in $Bi_2Sr_2CaCu_2O_{8+\delta}$, Science **295**, 466 (2002)

28.74   Y. Kohsaka, C. Taylor, K. Fujita, A. Schmidt, C. Lupien, T. Hanaguri, M. Azuma, M. Takano, H. Eisaki, H. Takagi, S. Uchida, J.C. Davis: An intrinsic bond-centered electronic glass with unidirectional domains in underdoped cuprates, Science **315**, 1380 (2007)

Kazuhiro Fujita

Condensed Matter Physics & Materials Science Dept.
Brookhaven National Laboratory
Upton, NY, USA
kfujita@bnl.gov

Kazuhiro Fujita received his PhD from the University of Tokyo, Japan in 2007. He has served as Postdoctoral Associate and Research Associate at Cornell University (2007–2015). In 2015, he was appointed Assistant Physicist at Brookhaven National Laboratory and became an Associate Physicist there in 2018.

Mohammad H. Hamidian

Dept. of Physics
Harvard University
Cambridge, MA, USA
m.hamidian@gmail.com

Mohammad H. Hamidian earned his BASc in Engineering Physics from the University of Toronto in 2004 and his PhD in Physics from Cornell University in 2011. After a postdoctoral fellowship at Cornell University he moved to Harvard University as a Research Associate in 2015.

Peter O. Sprau

Dept. of Physics
University of California, San Diego
La Jolla, CA, USA
psprau@physics.ucsd.edu

Peter Sprau received his Dipl.-Ing. Univ. in Nanostructure Technology from the Julius-Maximilians University Würzburg in 2012. He was a Visiting Scientist at UC Berkeley between 2009 and 2010. He received his PhD in Physics from Cornell University in 2017. Currently, he works on coherent x-ray methods as a postdoctoral scholar at UC San Diego.

Stephen D. Edkins

Dept. of Applied Physics
Stanford University
Stanford, CA, USA
edkins@stanford.edu

Stephen Edkins received his degrees in Natural Sciences from the University of Cambridge, followed by a PhD in Physics from the University of St. Andrews in 2016. From 2013 to 2017, he was a Visiting Scientist at Cornell University. He is currently an Urbanek Postdoctoral Fellow in the Department of Applied Physics at Stanford University.

J.C. Séamus Davis

Clarendon Laboratory
University of Oxford
Oxford, UK
Dept. of Physics
University College Cork
Cork, Ireland
jcseamusdavis@gmail.com

J.C. Séamus Davis earned his BSc (Physics) from University College Cork and PhD from the University of California – Berkeley. He was Professor of Physics at various universities, among them University of California – Berkeley (1993–2003), Cornell University (2003–2018) and St. Andrews University (2007–2018). In 2019 Davis became Professor of Physics at Oxford University, Professor of Quantum Physics at University College Cork and J.G. White Distinguished Emeritus Professor of Physics at Cornell University.

Part D | 28